

NASA CR-156696

SQT

(NASA-CR-156696)	SOLAR HEATING IN THE MARS	N78-20041
DUSTY ATMOSPHERE (Colorado Univ.)	61 p HC	
A04/MF A01	CSCL 03B	
		Unclas
		G3/91 07311

SOLAR HEATING IN THE MARS DUSTY ATMOSPHERE

Richard W. Zurek

Laboratory for Atmospheric and Space Physics

University of Colorado

Boulder, Colorado 80309



## I. Introduction

The Mariner 9 orbiter spacecraft observed that the Martian atmosphere was unexpectedly warm during the long-lived global dust storm of 1971. Subsequently, Gierasch and Goody (1972) noted that this was consistent with the direct absorption by airborne dust of a significant fraction of the incoming solar radiation. This suggested a simplistic radiative heating model in which the heating per unit mass,  $Q_m$ , is given by pure absorption of some fraction,  $\alpha_s$ , of the direct solar beam. Conrath (1975) has used such a model to examine the dissipation of the Martian 1971 dust storm.

If the dust particles are assumed to be spheres, Mie theory can be used to include the effects of radiative scattering by the dust if the size distribution and the wavelength dependent refractive index — particularly its complex component — are known. Moriyama (1974, 1975) has computed the solar heating and infrared cooling of the Martian atmosphere for various degrees of dustiness by assuming that the Martian dust particles are quartz particles having the same size distribution as terrestrial dust observed over northwest India.

Recently, however, analysis of the Mariner 9 ultraviolet spectrometer (UVS) observations have yielded new constraints

on the size distribution and on the complex refractive index of the airborne Martian dust. In this paper we estimate from various sources the complex refractive index in the solar spectral region ( $0.2 \leq \lambda \leq 5.0\mu\text{m}$ ). With this index and the size distribution estimated from the UVS data (Pang et al., 1976) we use Mie theory to compute the radiative parameters required for including radiative scattering in simplified radiative transfer approximations. These approximations then enable us to compute the wavelength-integrated solar heating for various dust-laden Martian atmospheres.

We have deferred to an appendix material discussing the relative merits of the delta-Eddington (Joseph et al., 1976), four-stream discrete ordinate (Liou, 1974) and four-component multiple stream methods for the optical parameter range appropriate to the Mars global dust storm. The calculations presented in the main body of the paper were computed using the delta-Eddington approximation.

## II. Complex Refractive Index for Solar Wavelengths

To include scattering in the radiative transfer equations, we need to know the normalized phase function  $\bar{P}(\cos \Theta)$  which describes the probability that a photon will be diverted by an angle  $\Theta$  from its original path during a single encounter with a nonabsorbing dust particle. For scattering which is azimuthally independent,  $\bar{P}(\cos \Theta)$  can be written  $\bar{P}(\mu, \mu')$  where  $\mu$  and  $\mu'$  are the direction cosines (with respect to the vertical) of the photon path before and after encounter with the dust particle. Since the dust may absorb the radiation as well as redirect it, the true scattering probability is

$$\hat{P}(\cos \Theta) = \tilde{\omega}_0 \bar{P}(\cos \Theta)$$

where the single scattering albedo  $\tilde{\omega}_0$  describes the probability that a photon is scattered rather than absorbed in a single dust particle encounter ( $\tilde{\omega}_0 = 1$  for pure--thus conservative--scattering).

If the scattering particles are spherical and the incident light is unpolarized, the phase function  $\hat{P}(\cos \Theta)$  can be computed from Mie theory if the complex refractive index  $m = m_r - i m_i$  and the ratio of the particle radius to the wavelength of the incident radiation are known for the particles. When the dust layer contains particles of several different sizes, the phase function must be weighted by the number of particles having that size and then averaged over all possible sizes. Thus, the phase function for a homogeneous dust layer where  $\dot{n}(r)$  is the number of particles per unit volume whose radii lie between  $r$  and  $r + \delta r$  is

ORIGINAL PAGE IS  
OF POOR QUALITY

given by

$$P(\cos \theta) = \frac{1}{N} \int_{r_1}^{r_2} \hat{P}(\cos \theta, r) n(r) dr, \quad (1)$$

where  $r_1$  and  $r_2$  are the limits of the size distribution and  $N$  is the total number of particles per unit volume. The dust layer is homogeneous if the refractive index and  $n(r)$  do not change horizontally or vertically throughout the dust layer. Although only single scattering has been mentioned above, the optical parameters required by the multiple scattering approximations to the radiative transfer equations discussed in section III can be generated from the phase function given by Eq. 1. For instance, the single scattering albedo for the size distribution  $n(r)$  is given by

$$\tilde{\omega}_0 = \frac{1}{2} \int_{-1}^1 P(\cos \theta) d(\cos \theta). \quad (2)$$

For the calculations presented here we have assumed that the particles in the dusty Martian atmosphere are spherical and that they can be described by the standard gamma (or two-parameter) distribution used by Pang et al. (1976):

$$n(r) = N \cdot (ab)^{\frac{2b-1}{b}} \cdot r^{\frac{1-3b}{b}} e^{-\frac{r}{ab}} / \Gamma[\frac{1-2b}{b}] \quad (3)$$

where  $\Gamma$  is the gamma function. Since

$$a = \frac{1}{G} \int_{r_1}^{r_2} r \pi r^2 n(r) dr \quad (3a)$$

$$b = \frac{1}{a^2 G} \int_{r_1}^{r_2} (r-a)^2 \pi r^2 n(r) dr, \quad (3b)$$

where  $G$  is the geometric cross-sectional area of particles per unit volume and is given by

$$G = \int_{r_1}^{r_2} \pi r^2 n(r) dr, \quad (3c)$$

the parameters  $a, b$  can be interpreted as the effective radius and the effective variance of the size distribution about  $a$ , respectively.

By varying  $a, b$  and the components  $m_r, m_i$  of the refractive index, Pang et al. (1976) estimated—on the basis of a least-error curve fitting of the Mie theory using Eqs. 1 and 3 to the phase functions constructed from the 1971 Mariner 9 dust storm data for two 10 nm bands centered at 268 and 305 nm—that

$$0.8 \leq a \leq 1.8 \mu m$$

$$0.2 \leq b \leq .$$

By studying these and other bands in the ultraviolet (UV) spectrum in the same manner, Pang and Ajello (1976) have determined "best" values for the refractive indices in the UV. Except for three uncertain points with wavelengths less than  $0.2 \mu m$ , their data have been reproduced by the crosses (+) plotted in Fig. 1 at the appropriate band centers.

To extend these results into the visible region, we have used the information provided by the isotropic single scattering albedos ( $\tilde{\omega}_s$ ) estimated from the Mariner 9 TV observations of limb haze during the Martian global dust storm (E. Anderson, communicated by C. B. Leovy). The values of  $\tilde{\omega}_s$  for the Martian tropics are shown in Table I. For optical depths characteristic of the active or quasi-steady Martian 1971 global dust storm ( $\tau_N \sim 1-2$ ), these  $\tilde{\omega}_s$  depend only slightly on the total optical depth  $\tau_N$ .

For isotropic scattering  $\hat{P}(\cos \theta) = \tilde{\omega}_s = \tilde{\omega}_s$  (a constant). Thus, the phase function given by Eq. 1 and its corresponding  $\tilde{\omega}_s$  are independent of particle size. If the actual scattering by the dust

is not isotropic, however, the  $\tilde{\omega}_*$  estimated from the data by assuming isotropy are size dependent. Assuming that the van de Hulst (1974) or two-stream similarity relations are valid, this apparent value of the isotropic  $\tilde{\omega}_*$  is related to the actual (non-isotropic) single scattering albedo  $\tilde{\omega}_0$  by

$$\tilde{\omega}_* = \frac{\tilde{\omega}_0 - g\tilde{\omega}_0}{1 - g\tilde{\omega}_0} \quad (4)$$

where  $g$  is the phase function asymmetry factor defined by

$$g = \frac{1}{2} \int_{-1}^1 P(\cos \theta), \cos \theta d(\cos \theta). \quad (5)$$

This dependence of the apparent  $\tilde{\omega}_*$  value on parameters generated from the actual phase function introduces the size dependence of  $\tilde{\omega}_*$ .

Thus, we proceed as follows: Utilizing the size distributions established by Pang et al. (1976), we use Mie theory with Eqs 1 and 2 to compute  $\tilde{\omega}_0$  at a specific wavelength but for a range of refractive indices. Then  $\tilde{\omega}_*$  is calculated from Eq. 4. Figure 2 shows various curves obtained for  $\lambda = 0.586 \mu\text{m}$ . Taking a value for  $\tilde{\omega}_*$  from Table I, we find  $\tilde{\omega}_*$  on a curve generated for the desired size distribution and real part  $m_r$  of the refractive index. From the abscissa of the graph we read the value for  $m_i$  and by moving vertically to the corresponding curve for  $\tilde{\omega}_0$ , we find the actual value for the single scattering albedo.

In this way we have established the six points indicated by (•) in Fig. 1. Because the curves in Fig. 2 have fairly shallow slopes with respect to  $m_i$ , the uncertainties tabulated in Table I yield greater uncertainties in  $m_i$  (shown by the error bars in Fig. 1).

Unfortunately, the  $\tilde{\omega}_*$  values listed in Table I depend on an absolute interpretation using vidicon data; as such, they are not very reliable. (The violet filter data are particularly dubious.) In spite of this, these  $\tilde{\omega}_*$  are consistent with values estimated by independently analyzing the Mariner 9 B-camera data (Leovy et al., 1972). Furthermore, they are consistent with values obtained from the geometric albedo of the Martian surface (primarily bright areas) from which the dust presumably came.

To compute these latter  $\tilde{\omega}_*$ , we relate  $\tilde{\omega}_*$  to the geometric albedo  $A_G$  for a homogeneous, isotropic semi-infinite medium:

$$A_G = \frac{2\pi}{S} \int_0^1 \int_0^1 I(\mu, \mu_0) \mu d\mu \mu_0 d\mu_0 \quad (6)$$

where

$$S = \int_0^1 \int_0^1 \mu I_s \delta(\mu, \mu_0) d\mu d\mu_0 = \frac{1}{2} I_s \quad (7)$$

with  $I_s \delta(\mu, \mu_0)$  being the solar intensity arriving at zenith angle  $\theta_0 = \cos^{-1} \mu_0$ . The diffuse intensity

$$I(\mu, \mu_0) = \frac{I_s}{\pi} \frac{\mu_0}{\mu + \mu_0} H(\mu, \tilde{\omega}_*) H(\mu_0, \tilde{\omega}_*) \frac{\tilde{\omega}_*}{4} \quad (8)$$

emerges at an angle  $\theta = \cos^{-1} \mu$ . The H functions are tabulated in Chandrasekhar (1960, p. 139). The resulting curve for  $A_G$  is shown in Fig. 3. Using de Vaucouleur's (1964) data for the geometric albedo, we find  $\tilde{\omega}_*$  from Fig. 3 and then use graphs similar to Fig. 2 to obtain the  $m_i$  values marked ( $\square$ ) in Fig. 1. We have used the geometric albedo here instead of the Bond albedo because  $A_G$  is the observed (from the earth) quantity.

Most of the calculations in this paper were done for one or both of the two size distributions listed in Table II. From Fig. 2



we see that these two size distributions more or less envelope the  $m_i$  estimates at visible and near-infrared wavelengths constructed from size distributions consistent with the work of Pang et al. (1976). Similar  $m_r$  values have been used for both size distributions. In the UV the real part of the refractive index is taken from Pang and Ajello's (1976) work; elsewhere  $m_r$  is taken to be consistent with Mead's (1970) estimates. The values used are shown in Fig. 1. The computed  $\tilde{\omega}_0$  or  $m_i$  values at visible and near-infrared wavelengths are insensitive to variations of  $m_r$  within the range  $1.55 \pm m_r \pm 1.80$ .

To demonstrate the consistency of the various data sources and methods, we have plotted  $\tilde{\omega}_0$ , which is one of the most critical optical parameters required to describe the radiative transfer in a dusty atmosphere, in Figs. 4 and 5 as constructed for size distributions S-II and S-I, respectively. Also plotted are the  $\tilde{\omega}_0$  computed from the refractive indices measured for two basalt samples, one studied by Pollack et al. (1973) and the other by Egan et al. (1975). Again, the S-II and S-I size distributions were used. Basalt is of interest because Adams and McCord (1969) have matched the geometric albedo of Mars in the visible and near-infrared spectrum with features of the reflectance curves of limonite-stained basalt. Differences between the optical properties of the two samples shown here are attributed to differences in chemical composition.

Figure 1 shows our best estimate for the complex refractive index at solar wavelengths. The UV data are taken as they stand except for the point at  $\lambda = 0.36\mu\text{m}$  whose low  $m_i$  value was required by Pang and Ajello (1976) to correctly model the Martian opposition effect. They refer to Mead (1970), but Mead's work does not by

itself impose such a stringently low value. The Mariner 9 TV data points are taken to be correct despite their possible bias. In the region  $0.65 \leq \lambda \leq 1.0 \mu\text{m}$ , we have used the refractive index estimated from our interpretation of the planetary geometric albedos. For  $\lambda \geq 1.0 \mu\text{m}$ , we have required  $m_i = 0.003$ , which is suggested by the basalt data. (See Appendix B.)

The two different curves in Fig. 1 for  $m_i$  at the visible and near-infrared wavelengths are a direct result of the size dependence of  $m_i$  when computed using  $\tilde{\omega}_*$  values derived from spacecraft or earth-based observations by assuming that scattering is isotropic in the dusty Martian atmosphere. In the following sections reference to the size distributions S-I and S-II will generally mean not only the distribution given by Eq. 3 with the size parameters listed in Table II, but will also imply the associated  $m_r$  and  $m_i$  values from Fig. 1.

ORIGINAL PAGE IS  
OF POOR QUALITY

### III. Radiative Transfer

To compute the vertical distribution of solar heating, we shall use simplified but reasonably accurate models of the multiple scattering radiative transfer equations. Because these models are computationally fast, they are exceptionally useful for parametric studies and can be easily incorporated into more general radiative equilibrium studies. Furthermore, our lack of detailed knowledge about the optical properties of the Martian dust and its spatial extent necessitates models which require only a few basic parameters.

In Appendix A we consider four simplified multiple scattering approximations: a four-stream discrete ordinate model (Liou, 1974), a four-stream multiple average-intensity model, and two versions of a delta-Eddington model. The accuracy of these are compared against an essentially exact doubling method for conditions appropriate to dusty Martian atmospheres.

The delta-Eddington method (Joseph et al., 1976) is a special combination of the usual Eddington and forward peak truncation approximations. More explicitly, the delta-Eddington azimuthally independent phase function is given by

$$P_{DE}(\cos \theta) = 4\pi f \delta(\mu - \mu') + (1-f)(1 + 3g_E \cos \theta) \quad (9)$$

where  $\theta$  is the scattering angle between the incident and emergent directions identified by the direction cosines  $\mu$  and  $\mu'$ , respectively, while  $f$  is the fractional scattering partitioned to the forward peak described by the delta function  $\delta(\mu - \mu')$ . The factor  $g_E$  is

related to the phase function asymmetry factor by

$$g = \frac{1}{2} \int_{-1}^1 \cos \theta P_{DE}(\cos \theta) d(\cos \theta) = f + (1-f) g_E. \quad (10)$$

If the optical depth and single scattering albedo are scaled as

$$\tau_E = (1 - \tilde{\omega}_0 f) \tau \quad (11)$$

$$\tilde{\omega}_E = (1-f) \tilde{\omega}_0 / (1 - \tilde{\omega}_0 f), \quad (12)$$

the delta-Eddington radiative transfer solution can be obtained from the standard Eddington approximation simply by replacing  $\tau$ ,  $\tilde{\omega}_0$ ,  $g$  by  $\tau_E$ ,  $\tilde{\omega}_E$ ,  $g_E$ , all of which can be computed once  $f$  is known. Since

$$f = \frac{1}{2} \int_{-1}^1 P_2(\cos \theta) P_{DE}(\cos \theta) d(\cos \theta) \quad (13)$$

where  $P_l$  denotes the  $l$ th Legendre polynomial, we can set  $f = \omega_2/5$  if  $\omega_2$  is the coefficient of  $P_2$  in a Legendre polynomial expansion of the normalized phase function. If the actual phase function has the same second moment as the Henyey-Greenstein function, then  $f = g^2$ .

The results shown in this and subsequent sections have been computed using the delta-Eddington method with  $f = g^2$  where  $g$  and  $\tilde{\omega}_0$  are determined from a Mie calculation using the refractive indices of Fig. 1 with the appropriate size distribution listed in Table II. Of the four methods examined in Appendix A, the  $f = g^2$  version of the delta-Eddington had the most consistently small errors when computing radiative fluxes and flux divergences. Furthermore, its overall error was smallest for the important small solar zenith angles. Each of the other methods had regions in  $\tau, \mu$  space where they were as good or better than the delta-

Eddington approximation, but the discrete and multiple intensity methods in particular tended to have uncomfortably large errors for nearly vertically incident insolation.

In the calculations that follow, the Martian atmosphere was assumed to be a plane-parallel atmosphere containing a vertically and horizontally homogeneous dust layer extending to the ground. The boundary conditions specified were that the diffuse downward radiation vanish at the top of the dust layer ( $\tau = 0$ ), assuming that absorption by  $\text{CO}_2$  in the solar spectral region is negligible, and that

$$F\uparrow(\tau_N, \mu_0) = A_s F\downarrow(\tau_N, \mu_0), \quad (14)$$

where  $\tau_N$  is the total vertical extinction optical depth of the dust cloud,  $A_s$  is the surface albedo, and  $\mu_0$  is the cosine of the solar zenith angle, while  $F\uparrow$  and  $F\downarrow$  are the upward and downward radiative fluxes, respectively.

To determine the surface albedo, we compute the Bond albedo for a homogeneous, isotropic, semi-infinite atmosphere:

$$A_B = \frac{4\pi}{S} \int_0^1 \int_0^1 I(\mu, \mu_0) \mu d\mu d\mu_0 \quad (15)$$

where  $S$  and  $I(\mu, \mu_0)$  are given by Eq. 7 and Eq. 8, respectively. The resulting curves for  $A_B(\tilde{\omega}_*)$  and the ratio  $A_B/A_G$ , known as the phase integral, are shown in Fig. 3. The Bond albedo is the appropriate surface albedo because it represents the ratio of the flux reflected in all directions from the planar surface to the flux intercepted by that surface. Using Fig. 3 and the  $\tilde{\omega}_*$  computed for the S-II size distribution (including the associated refractive

indices from Fig. 1), we obtain the surface albedo shown in Fig. 6, except that we have held the ground albedo constant at  $A_g = 0.480$  for wavelengths beyond  $1.4\mu m$ .

Obviously, there are large uncertainties inherent in this derivation for  $A_g$ . The consistency of the  $\tilde{w}_0$  values computed from the geometric albedos and of those derived from the Mariner 9 TV data suggest that the dust in the Martian atmosphere is the same as the dust on the surface. If they do have the same size distribution and the same refractive indices, there is no need for a surface albedo at all. The lower boundary condition given by Eq. 14 could be replaced by

$$F\uparrow(\tau_N, \mu_0) = 0. \quad \text{at } \tau_N \rightarrow \infty. \quad (16)$$

As we shall show in the next section, inserting the Bond albedo constructed using Eq. 15 into Eq. 14 with a finite  $\tau_N$  does indeed yield practically the same radiative fluxes and heating rates for  $\tau \lesssim \tau_N$  as does utilizing Eq. 16 directly for a much larger  $\tau_N$ .

However, the dust on the surface may not be the same as the dust particles that become airborne. They may have different size distributions or the dust on the surface may be mixed with ice. Furthermore, the airborne dust in a global dust storm need not have originated at the surface immediately beneath it.

If the two dust regimes are optically different, than Eq. 14 gives the appropriate lower boundary condition, but the ground albedo in such a case may well be different from that shown in Fig. 6.

ORIGINAL PAGE IS  
OF POOR QUALITY

## IV. Solar Heating

To examine the vertical distribution of solar heating due to dust in the Martian atmosphere, we first define the following quantities:

$$Q_{\tau}(\Delta_s) = \int_{\Delta_s} \frac{dF_{NET}}{d\tau} d\lambda \quad (17)$$

$$Q_z = -\frac{dT}{dz} Q_{\tau} \quad (18)$$

$$Q_m = \frac{1}{\rho} Q_z \quad (19)$$

where  $\tau$  is the vertical extinction optical depth for dust evaluated at  $\lambda = 0.586\mu\text{m}$ , while  $\Delta_s$  represents the interval  $0.2 \leq \lambda \leq 5.0\mu\text{m}$  and  $Q_z$ ,  $Q_m$  are the heating rates per unit volume and per unit mass, respectively.  $F_{NET}$  is the net radiative flux and includes both the direct and diffuse solar contributions, while  $\rho$  is the mass density of air ( $\text{CO}_2$  in this case).  $Q_{\tau}$  is a useful measure of the total solar heating rate because it is independent of any vertical redistribution of the dust as long as the total optical depth remains the same. Local heating rates ( $Q_z, Q_m$ ), of course, will vary according to the local dust concentration.

The integral in Eq. 17 was evaluated by a 32-point Gauss-Legendre quadrature for  $\ln(.2) \leq (\xi = \ln \lambda) \leq \ln(5.0\mu\text{m})$ . Since the global dust storms originate during the Martian southern hemispheric summer, the solar constant was evaluated for a planetary distance of 1.45 A.U., where it has the value  $64.6 \text{ mw cm}^{-2}$ . ( $1 \text{ mw} = 10^4 \text{ ergs sec}^{-1}$ .) The wavelength distribution of the solar intensity was taken from Allen(1973). The

optical parameters ( $\tilde{w}_0$ ,  $g$ ,  $\sigma_{\text{ext}}$ ) were computed for the quadrature wavelengths using the refractive indices in Fig. 1; these parameters are listed in Appendix B. Unless otherwise noted, the surface albedo AS-II, shown in Fig. 6, was used for all calculations.

$Q_\tau(A_s)$  is plotted in Fig. 7 as a function of optical depth  $\tau$  and solar zenith angle  $\cos^{-1}\mu_0$ . To insure that the solar heating rate being averaged over wavelength refers to a single height level, the optical depth for a single wavelength has been scaled with respect to  $\tau$ , the optical depth at  $\lambda = 0.586\mu\text{m}$ . Since

$$\frac{d\tau}{dz} = -n_D \sigma_*$$
(20)

where  $n_D$  is the number density of dust particles and  $\sigma_*$  is the extinction cross-section for  $\lambda = 0.586\mu\text{m}$  (assumed constant), this required that the integral in Eq. 17 be evaluated by summing over the quadrature points using values of  $\frac{dF_{\text{NET}}}{d\tau}(\lambda, \tau_\lambda)$  for which

$$\tau_\lambda = \frac{\sigma_{\text{EXT}}(\lambda)}{\sigma_*} \tau.$$
(21)

Thus,

$$\frac{dF_{\text{NET}}}{d\tau} = \frac{d\tau_\lambda}{d\tau} \frac{dF_{\text{NET}}}{d\tau_\lambda} = \frac{\sigma_{\text{EXT}}(\lambda)}{\sigma_*} \frac{dF_{\text{NET}}}{d\tau_\lambda}.$$
(22)

The solid curves in Fig. 7 assume that the dust on the surface is optically the same as the dust in the atmosphere so that the atmosphere-ground system can be treated as a homogeneous semi-infinite medium. The other curves show that placing a physical surface with the ground albedo shown in Fig. 6 at finite optical depths typical of the Martian global dust storm ( $\tau_H \sim 1-2$ , Leovy et al., 1972) changes the solar heating per



unit optical depth by less than 5% for  $\mu_0 = 1.0$  and by even smaller margins for smaller  $\mu_0$ . In fact, for  $\mu_0 \leq 0.6$ , the curves for  $\tau_N = 2.0, 1.5$ , and  $100$  agree within 1%. The computed net fluxes also change by only 1-5%, and the largest differences again occur when  $\mu_0 = 1.0$ . This good agreement is not unfounded since we have used the same basic assumption--that the surface and airborne dust particles are optically the same--to construct the ground albedo curve in Fig. 6. As long as this assumption is true, the  $Q_\tau$  values on the solid curves will differ from the curves computed for a given finite  $\tau_N$  by less than 6% for  $\tau \neq \tau_N$ .

As shown by Fig. 8, the relative errors of the infinite versus finite  $\tau_N$  curves for the solar heating contributed by different segments of the solar spectrum are comparable to those for the heating integrated over all of  $\Delta_s$ . Thus, the agreement between the curves shown in Fig. 7 is not a result of the cancellation of much larger changes contributed by different wavelength intervals. Figure 8 also shows that the largest contribution by far to the total solar heating rate comes from the visible region ( $\Delta_{vis}: 0.4 \leq \lambda \leq 1.0 \mu m$ ), followed by the near-infrared ( $\Delta_{NIR}: 1.0 \leq \lambda \leq 2.5 \mu m$ ). The region beyond  $2.5 \mu m$  contributes very little to the integrated solar heating.

Comparing curves in Fig. 9 reveals that there is little difference between  $Q_\tau(\Delta_s)$  computed from the S-I rather than the S-II size distribution even though the contributions from the various spectral regions differ significantly. The increased visible region contribution for S-I--due to the larger  $m_1$

indices associated with the S-I size distribution at visible wavelengths--is almost exactly compensated by the decreased near-infrared contribution--due to the generally smaller ratio of particle radius to wavelength for the S-I distribution--as compared to the S-II results. Relative differences in  $Q_T(\Delta_s)$  computed for these two distributions are less than 3% while the corresponding fluxes differ by a similar amount. Usually, differences resulting from acceptable changes in the size distributions are much smaller than differences arising from possible surface albedo changes. As shown in Fig. 10, for instance, reducing the ground albedo by 50% decreases the  $Q_T(\Delta_s)$  values for  $\mu_0 = 1.0$  by 10% at the top of the dust cloud and by almost 20% at  $\tau_N = 1.5$ .

Because the visible region so dominates the integrated solar heating, replacing the surface albedo AS-II by the constant value  $A_s = 0.30$  does not significantly alter the results (within 4%) for  $Q_T(\Delta_s)$ . The corresponding net fluxes, however, change systematically by 5-12%. As one might expect, most of this difference is associated with the upward flux  $F\uparrow$ . Indeed,  $F\uparrow(\tau_N)$  decreases by less than 4% when  $A_s = .30$  replaces AS-II while  $F\uparrow(0)$  decreases by as much as 15%. The constant surface albedo increases the UV contribution to  $Q_T(\Delta_s)$ , but the decrease of the near-IR contribution compensates this increase almost exactly.

We can define a solar heating rate for the entire dust layer by

$$\hat{Q}_\tau = \int_0^{\tau_N} Q_\tau(\Delta_s) d\tau = F_{NET}(\tau_N) - F_{NET}(0). \quad (23)$$

The variation of  $\hat{Q}_\tau$  with  $\mu_0$  is shown in Fig. 11. Again, we see that the results are quite similar when  $\tau_N = 1.5$  for  $\hat{Q}_\tau$  values computed from either the S-I or S-II size distributions, but that  $\hat{Q}_\tau$  is substantially reduced for large  $\mu_0$  over a less-reflecting surface. Also shown in Fig. 11 is the layer heating rate when  $\tau_N$  is reduced by a factor of 10.

As shown in Fig. 12,  $Q_\tau(\Delta_s)$  varies linearly with  $\tau$  for  $\mu_0 \gtrsim 0.4$  when  $\tau_N = 0.15$ . Although the  $Q_\tau(\Delta_s)$  rates are comparable with the rates obtained for  $\tau_N = 1.5$ , the volume and mass heating rates will decrease by an order of magnitude because there is less dust to do the heating when  $\tau_N = 0.15$ .

Figure 12 shows the solar heating rates as a function of  $\tau$  and  $\mu_0$  when  $\tau_N = 0.15$ . Again, the two different boundary conditions given by Eqs. 14 and 16 give similar results. The largest error between the two is  $\sim 6\%$ . Figure 13 shows the effect of replacing the AS-II ground albedo by the constant  $A_s = .30$ . The relative errors have the same sign as for the comparison when  $\tau_N = 1.5$ , but are smaller in magnitude by a factor of two or so. Reducing the ground albedo by half, however, changes the solar heating rates by  $\sim 20\%$  throughout the dust column.

To translate the solar heating rates per unit optical depth into heating rates per unit volume ( $Q_z$ ) or unit mass ( $\dot{Q}_m$ ); we need to know the vertical distribution of the airborne dust.

Dust was detected as high as 70 km during the 1971 Martian global dust storm (Ajello et al., 1976). Assuming that the dust was uniformly mixed by volume throughout the atmosphere, Eq. 20 can be integrated to yield

$$\tau(z) = c \cdot p$$

where  $p$  denotes pressure and the constant  $c$  is given by

$$c = \frac{q \sigma_s}{g_p m_{CO_2}} = \frac{\tau_N}{p_s} \quad (24)$$

where  $q = n_D/n_A$  is the volume mixing ratio,  $g_p$  is Martian gravity,  $m_{CO_2} = 7.3 \times 10^{-23}$  gm per molecule ( $CO_2$ ), and  $p_s$  is the Martian surface pressure (taken to be 5 mb). Since the total optical depth during the dust storm is  $\tau_N \sim 1-2$  (Leovy et al., 1972),  $c \sim 0.3 \text{ mb}^{-1}$ . This implies that  $q \sim 1.3 \times 10^{-16}$  dust particles per air molecule for the S-II size distribution and  $q \sim .8 \times 10^{-15}$  for S-I. The number of dust particles in an atmospheric column is then  $\tau_N / \sigma_s$ , which is  $1.5 \times 10^8 \text{ cm}^{-2}$  for the S-I size distribution and  $2.4 \times 10^7$  for S-II.

To compute the solar heating per unit mass shown in Fig. 14, we multiply the  $\tau_N = 1.5$  curves in Fig. 7 by

$$-\frac{1}{g} \frac{d\tau}{dz} = g_p \cdot c,$$

ORIGINAL PAGE IS  
OF POOR QUALITY

which is constant for the the uniformly mixed dust. Thus, the solar heating per unit mass is fairly constant with height for  $\mu_0 \sim 1.0$ . The decrease near the surface is more pronounced at all  $\mu_0$  as  $\tau_N$  increases beyond  $\tau_N = 1.5$  (see Fig. 7). If we denote averages over  $\mu_0$  (global averages) by an overbar ( $\bar{Q}_m$ , for example), we see that the averaged solar heating rate decreases significantly in the lower part of the dust layer. Furthermore,

$Q_m(\mu_0 = 0.4)$  is a good approximation to the averaged heating rate above  $z = 1.0$  ( $\tau \sim 0.6$ ) when  $\tau_N = 1.5$ .

Specific values of the solar heating per unit mass,  $Q_m(\mu_0)$ , and the averaged value  $\bar{Q}_m$  are tabulated in Table III for representative heights and for  $\tau_N = 1.5, 0.15$ . To convert the units given in the table ( $\text{mw gm}^{-1}$ ) to  $\text{K day}^{-1}$ , the numbers should be multiplied by  $\sim 100$ . Thus,  $Q_m$  may exceed  $50\text{K day}^{-1}$  while  $Q_m(\mu_0 = 1.0)$  may reach  $90\text{K day}^{-1}$  when  $\tau_N = 1.5$ . Even in the optically thin case when  $\tau_N = 0.15$ , heating rates of nearly  $10\text{K day}^{-1}$  may occur when the sun is overhead.

In Table IV we have shown the partitioning of the incident solar radiation into the layer heating  $\hat{Q}_m$  (per unit mass), the upward flux out of the layer,  $F\uparrow(0)$ , and the net flux into the surface  $F_{\text{src}}$ . During the Martian global dust storm some 20% of the incoming solar radiation was absorbed by the dusty atmosphere, and the flux to the surface was decreased by one-third as compared to the optically thin case. (This latter result assumes that the ground albedo has not been changed by the dynamically active dust storm.) The upward flux out of the dusty atmosphere remains the same. Thus, we would expect the atmosphere to become warmer during a Martian global dust storm, as the Mariner 9 observations have shown that it did. We cannot theoretically determine how much warmer the dusty atmosphere should become, however, until the dust contribution to the infrared cooling is known.

## V. Summary and Discussion

Due to radiative scattering, the solar heating per unit mass of a dusty Martian atmosphere in which the dust is uniformly mixed is surprisingly constant with height if the total extinction optical depth  $\tau_N \lesssim 1.5$ . This result was suggested long ago by the Mariner 9 IRIS temperature observations of the 1971 global dust storm. The heating rates per unit mass derived in the previous section are as large as 90 K/day when  $\tau_N = 1.5$ .

The solar heating derived by Moriyama (1975) for the Martian global dust storm is considerably larger than that computed here and the heating attains a prominent maximum in the middle layers of the dust cloud. Moriyama chose  $m_i = 0.033$  in the visible region since this value produced a single scattering albedo of 0.7 for  $\lambda \sim 0.6\mu\text{m}$ . The value 0.7, however, assumes isotropic scattering (Leovy *et al.*, 1972) and the corresponding non-isotropic  $\tilde{\omega}_0$  is close to 0.9 (see Fig. 2). The increased absorption resulting from this unrealistically large  $m_i$  value accounts for his enhanced heating maximum in the middle layers of the dust cloud and the decreased solar heating near the ground. Our results do support his conclusion, however, that even optically thin dust layers can produce heating rates of a few degrees per day.

If the van de Hulst similarity relations are valid, the largest uncertainty affecting the results given here is probably the ground albedo in the visible spectrum, although assuming vertical homogeneity may turn out to be equally damaging.

To complete the description of the radiation field in a dusty Martian atmosphere, the vertical distribution of the infrared cooling by the combined dust-CO<sub>2</sub> system needs to be calculated. As pointed out by Moriyama (1974), most of the large solar heating of the dust-laden atmosphere is probably balanced by enhanced infrared cooling due to the airborne dust.

ORIGINAL PAGE IS  
OF POOR QUALITY

Acknowledgments. I wish to thank Drs. R. E. Dickinson, C. W. Hord, and C. B. Leovy for their valuable discussion and assistance. This work was supported by NASA grant NAS 5-22440, while computer time for this research was obtained from the National Center for Atmospheric Research, which is sponsored by the National Science Foundation.



## APPENDIX A

Comparing approximations to the radiative transfer equation  
for conditions appropriate to Mars

We consider here four approximations to the radiative transfer equation: a four-stream discrete ordinate method, a four component multiple average-intensity method, and two versions of the delta-Eddington method described in section III.

Both delta-Eddington methods,  $DE(g^2)$  and  $DE(\omega_2/5)$ , assume that the fraction  $f$  of the total scattering partitioned to the forward peak of the delta-Eddington phase function (Eq. 9) is related to the second moment of the normalized phase function:

$$\omega_2 = \frac{5}{2} \int_{-1}^1 P_2(\cos \theta) P(\cos \theta) d(\cos \theta) = 5f \quad (A1)$$

For the  $DE(\omega_2/5)$  version,  $f$  is computed from the Legendre polynomial expansion of the normalized phase function generated by a Mie program for the appropriate size distribution and refractive index at the given wavelength. The  $DE(g^2)$  version, however, assumes that the actual phase function  $P(\cos \theta)$  has the same second moment as the Henyey-Greenstein phase distribution:

$$f = \frac{\omega_2}{5} (H-G) = g^2$$

where  $g$  is the asymmetry factor defined by Eq. 5. For both models

ORIGINAL PAGE IS  
OF POOR QUALITY

the asymmetry factor is computed from Mie theory, again using a given size distribution and the appropriate refractive index for the specified wavelengths.

In the four-stream discrete ordinate method (denoted FS) the angular intensity distribution for a given wavelength,  $I_\lambda(\tau, \mu)$ , is replaced by  $2J=4$  intensity streams, which are the  $I_\lambda$  evaluated at the  $2J$  Gauss-Legendre quadrature points. Thus, the radiative equation of transfer for solar wavelengths becomes discretized with respect to the scattered and incident direction cosines

$\mu, \mu'$ :

$$\mu_i \frac{dI(\tau, \mu_i)}{d\tau} = I(\tau, \mu_i) - \frac{\tilde{\omega}_0}{2} \sum_{j=1}^{2J} a_j P(\mu_i, \mu_j) I(\tau, \mu_j) - P(\mu_i, \mu_0) \frac{\tilde{\omega}_0}{4} I_s e^{-\tau/\mu_0} \quad (A2)$$

where  $P(\mu, \mu')$  is the normalized phase function,  $\tilde{\omega}_0$  is the single scattering albedo,  $\mu_0$  is the cosine of the solar zenith angle, and  $I_s$  is the solar intensity. The source function integral has been replaced by a  $2J$  Gaussian quadrature with quadrature weights  $a_j$  at the quadrature points  $\mu_j$ . The above equation holds for a specific wavelength although the  $\lambda$  subscript has been suppressed. When  $J = 1$  or  $2$ , algebraic formulas can be obtained for the different intensity streams  $I(\tau, \mu_i)$ ,  $i = 1, 2J$ . (Liou, 1974; note, however, that his formula assumes a different lower boundary condition than Eq. 14 in section III.)

Essentially, the four-stream method assumes that the phase function is given by the first four terms of its Legendre polynomial expansion:

$$P(\cos \theta) = \sum_{n=0}^{2J-1=3} \omega_n P_n(\cos \theta) = P(\mu, \mu') = \sum_{n=0}^3 \omega_n P_n(\mu) P_n(\mu'). \quad (A3)$$

This severe truncation of the phase function expansion leads to negative values of  $P(\cos \theta)$  for some scattering angles. This unrealistic result may account for the suprisingly large errors of the FS model for nearly vertical insolation ( $\mu_0 \sim 1.$ ).

This severe truncation of the phase function expansion for a small number of intensity streams can be circumvented if we assume that the angular intensity distribution is constant over the  $2J$  intervals  $\alpha_i \leq \mu \leq \beta_i$  covering the range  $-1. \leq \mu \leq +1.$  We can still use the discrete ordinate formulas if we make the following substitutions:

$$\begin{aligned} \alpha_i &\longrightarrow \Delta_i \equiv \beta_i - \alpha_i \\ P(\mu_i, \mu_j) &\longrightarrow \frac{1}{\Delta_i} \int_{\alpha_i}^{\beta_i} d\mu \int_{\alpha_j}^{\beta_j} P(\mu, \xi) d\xi \\ \mu_i &\longrightarrow \bar{\mu}_i \equiv \frac{1}{2} (\beta_i + \alpha_i) \\ I(\tau, \mu_i) &\longrightarrow I_i(\tau) \end{aligned}$$

ORIGINAL PAGE IS  
OF POOR QUALITY

where the quadrature intensity streams are replaced by intensity components  $I_i(\tau)$ , assumed to be the constant value of  $I(\tau, \mu)$  on the interval  $\alpha_i \leq \mu \leq \beta_i$ . Since energy conservation requires that

$$\frac{1}{2} \sum_{i=1}^{2J} \Delta_i = 1,$$

the multiple intensity method used here assumed that  $\Delta'_i = \alpha_i$ , the Gaussian quadrature weights. Since  $\alpha_1 = -1.$  and  $\beta_{2J} = \beta_1 = 1.$ , the remaining  $\alpha_i, \beta_i$  are specified once the  $\Delta_i$  are known; this also predetermines the median points  $\bar{\mu}_i$ .

As shown by Fig. A-1 through A-4, this multiple average-intensity method (denoted FMS) models the shape of the net flux

divergence as it varies with optical depth quite well, but the magnitude is too large when compared with the Doubling method results. Generally, the FMS error is comparable to that produced by the discrete ordinate method.

Figures A-1 through A-10 compare either fluxes or net flux divergences (with respect to optical depth) as computed by the radiative approximations with the same quantities computed by the Doubling method. The Doubling method used here utilizes 22 terms of the Legendre polynomial expansion of the phase function generated by a Mie calculation using the S-II size distribution for  $\tau_N = 1.5$  and the S-I distribution with its slightly smaller particles for  $\tau_N = 0.15$ . (In this section the vertical optical depth  $\tau$  applies to the given wavelength.) Interchanging the size distributions for these two cases does not significantly change the results given here as long as the corresponding refractive indices are taken from Fig. 1. All calculations shown in the figures, except for Fig. A-8, are computed for the wavelength  $\lambda = 0.586 \mu m$  and a surface albedo  $A_s = 0.2788$ , which are representative of the important visible wavelengths. In all cases the incident solar flux has arbitrarily been set equal to  $SF = 1.0$ .

The two delta-Eddington methods generally agree quite well with each other; in Fig. A-9, for instance, they are indistinguishable for  $\mu_0 = 0.6$ . Both approximations are usually significantly better than either of the four-stream models--especially for the larger  $\mu_0$  values. For  $\tau_N \sim 1.0$ , the intensity stream models are distinctly better when computing flux divergences only for  $\mu_0 \sim 0.6$ . As noted above, both are considerably worse than

ORIGINAL PAGE IS  
OF POOR QUALITY

$DE(g^2)$  when  $\mu_o = 1.0$ . Figures A-6 and A-7 show relative errors (as compared to the Doubling method) of the various approximations when computing the downward flux to the surface or when calculating the upward flux at the top of the dusty atmosphere. Again, the delta-Eddington methods are generally better for large  $\mu_o$ , and  $DE(g^2)$  is significantly closer to the Doubling method result than  $DE(\omega_2/5)$  for  $\mu_o \sim 1.0$ . The FS model, however, is quite good for all  $\mu_o$  when computing the downward flux at the surface.

The relative errors when computing the layer heating rate, defined as  $F_{NET}(\tau_N) - F_{NET}(0)$ , are shown in Fig. A-5 for  $\tau_N = 1.5$  and in Fig. A-10 for  $\tau_N = 0.15$ . Both Figs. A-5 and A-7 show the nature of the four-stream error, which can become uncomfortably large for  $\mu_o \sim 1.0$ .

Figure A-8 shows the flux divergence computed at  $\lambda = 0.201 \mu m$  for  $\tau_N = 1.5$  and  $A_s = 0.03$ . Again the delta-Eddington approximations are best. However, the multiple average-intensity method is noticeably better than the discrete ordinate method for the stronger absorption ( $\tilde{\omega}_o \sim 0.6$ ) at the ultraviolet wavelengths.

The FMS method is far worse than the others for the almost optically thin case where  $\tau_N = 0.15$ . When  $\mu_o = 1.0$ , relative errors in the flux divergence computed from the four-stream multiple average-intensity method can reach 35%. The corresponding error for the layer heating rate can exceed 30%, as shown in Fig. A-10. The four-stream discrete ordinate method, however, is competitive with the delta-Eddington approximation when  $\tau_N = 0.15$ .

Thus, we conclude that for conditions appropriate to the dusty Martian atmosphere the delta-Eddington  $DE(g^2)$  method is adequate and is the best of the four methods examined above. This is clearly true for the fluxes and flux divergences (with respect to optical depth) computed for  $\mu_0 > 0.6$ . Furthermore, the  $DE(g^2)$  method requires the fewest number of optical parameters ( $\tilde{\omega}_0$ ,  $g$ ,  $A_s$ ,  $\tau_N$ , and  $\sigma_{ext}$ , the extinction cross-section) of the four methods, and it is almost an order of magnitude faster computationally than the four-stream methods.

The four-stream discrete ordinate method is noticeably better for  $\mu_0 \sim 0.6$ , while the four-stream multiple average-intensity model may be useful for certain long slant optical paths or at strongly absorbing ( $\tilde{\omega}_0 \lesssim .5$ ) wavelengths.

We again emphasize that the comparisons are for the size distributions and refractive indices (at solar wavelengths) thought to be appropriate for Martian dusty atmospheres. However, the general trends discussed above indicate that the delta-Eddington method should be considered whenever one needs a computationally fast, simple yet realistic approximation to the full radiative transfer equations applied to scattering atmospheres.

ORIGINAL PAGE IS  
OF POOR QUALITY

## Appendix B

Table B-I lists the optical parameters used by the delta-Eddington approximation to the radiative transfer equations. These parameters were generated using the S-I and S-II size distributions from Table II with the tabulated refractive indices at the listed quadrature wavelengths. The refractive indices listed below (and shown in Fig. 1) were obtained by linear interpolation over wavelength on the values given in Table B-II.

TABLE B-I

Optical parameters and constants at the quadrature wavelengths.  $S_\lambda$  is the product of the quadrature weight and the solar intensity at the quadrature wavelength. The solar insolation as a function of wavelength was taken from Allen (1973) and adjusted to a planetary distance (for Mars southern summer) of 1.45 A.U. The 32 Gauss-Legendre quadrature points were taken for the interval  $\ln(0.2\mu\text{m}) \leq \ln \lambda \leq \ln(5.0\mu\text{m})$ . The scaling factor  $r = \sigma_{\text{EXT}} / \sigma_*$  is also listed. All parameters are associated with or generated from either the S-I or S-II size distributions.

S - I							
$\lambda(\mu\text{m})$	$\tilde{\omega}_0$	$g$	$\sigma_{\text{EXT}}(\mu\text{m}^2)$	$r$	$S_\lambda(\text{ergs/sec cm}^2)$	$m_r$	$m_i$
.201	.618	.845	.895	.901	4.95	1.80	.02200
.205	.618	.844	.894	.900	16.64	1.80	.02200
.212	.620	.838	.894	.900	41.51	1.81	.02192
.222	.631	.824	.898	.904	86.42	1.85	.02126
.236	.644	.815	.901	.907	141.07	1.85	.01967
.255	.656	.805	.908	.914	354.73	1.85	.01877
.278	.690	.777	.916	.922	920.57	1.85	.01529
.308	.741	.752	.917	.923	3007.70	1.84	.01134
.344	.858	.715	.921	.927	5614.71	1.75	.00507
.388	.856	.701	.947	.954	7633.26	1.75	.00585
.442	.855	.685	.967	.974	16527.19	1.75	.00630
.508	.872	.675	.992	.999	20789.93	1.75	.00630
.586	.886	.658	.993	1.000	23149.82	1.75	.00619
.680	.948	.621	1.031	1.038	23135.47	1.75	.00273
.793	.950	.580	1.043	1.050	21569.70	1.75	.00259
.925	.959	.626	1.056	1.063	18816.43	1.65	.00300
1.081	.965	.620	1.082	1.090	15888.35	1.65	.00300
1.262	.969	.611	1.101	1.109	13137.76	1.65	.00300
1.470	.973	.610	1.089	1.097	10650.49	↓	↓
1.706	.977	.605	1.089	1.097	7936.04		
1.970	.979	.607	1.055	1.062	5213.59		
2.261	.982	.607	1.007	1.014	3791.23		
2.575	.983	.607	.944	.951	2359.92		
2.907	.984	.605	.871	.877	1578.33		
3.249	.985	.602	.792	.798	1136.04		
3.592	.985	.597	.715	.720	816.64		
3.924	.986	.591	.643	.648	502.18		
4.232	.986	.585	.581	.585	344.50		

(cont.)

ORIGINAL PAGE IS  
OF POOR QUALITY



TABLE B-I (cont.)

4.503	.986	.578	.530	.534	244.42	1.65	.00300
4.724	.986	.573	.492	.495	157.84	1.65	.00300
4.886	.986	.569	.465	.468	89.12	1.65	.00300
4.978	.986	.566	.451	.454	34.90	1.65	.00300

## S - II

.201	.579	.892	5.76	.919	4.95	1.80	.02200
.205	.580	.890	5.76	.919	16.64	1.80	.02200
.212	.582	.888	5.77	.920	41.51	1.81	.02192
.222	.589	.879	5.79	.923	86.42	1.85	.02126
.236	.597	.873	5.81	.926	141.07	1.85	.01967
.255	.606	.866	5.83	.930	354.73	1.85	.01877
.278	.634	.845	5.86	.935	920.57	1.85	.01529
.308	.681	.816	5.88	.938	3007.70	1.84	.01134
.344	.812	.770	5.94	.948	5614.71	1.75	.00493
.388	.847	.749	5.98	.953	7633.26	1.75	.00415
.442	.871	.730	6.05	.966	16527.19	1.75	.00367
.508	.885	.715	6.18	.986	20789.93	1.75	.00359
.586	.899	.701	6.27	1.000	23149.82	1.75	.00344
.680	.955	.660	6.39	1.019	23135.47	1.75	.00157
.793	.958	.634	6.61	1.054	21569.70	1.75	.00149
.925	.960	.628	6.62	1.056	18816.43	1.75	.00188
1.081	.955	.618	6.88	1.097	15888.35	1.73	.00225
1.262	.956	.611	7.12	1.135	13137.76	1.70	.00257
1.470	.962	.614	7.29	1.163	10650.49	1.66	.00295
1.706	.966	.606	7.66	1.222	7936.04	1.65	.00300
1.970	.971	.604	7.85	1.253	5213.59	1.65	.00300
2.261	.976	.605	8.00	1.277	3791.23	1.65	.00300
2.575	.979	.609	8.05	1.285	2359.92	↓	↓
2.907	.981	.612	7.98	1.273	1578.33		
3.249	.983	.615	7.76	1.238	1136.04		
3.592	.984	.616	7.44	1.187	816.64		
3.924	.985	.616	7.05	1.125	502.18		
4.232	.986	.613	6.66	1.062	344.50		
4.503	.986	.611	6.30	1.004	244.42		
4.724	.986	.608	5.99	.956	157.84		
4.886	.986	.606	5.78	.921	89.12		
4.978	.986	.604	5.65	.901	34.90	1.65	.00300

TABLE B-II

Refractive indices for the solar wavelengths  $0.2\mu\text{m} \leq \lambda \leq 5.0\mu\text{m}$  were generated from the following values using linear interpolation over wavelength  $\lambda$ . The UV data (first section) are from Pang and Ajello (1976). All values listed here are shown in Fig. 1.

$\lambda$ ( $\mu\text{m}$ ):	.210	.220	.233	.243	.253	.269	.280	.305	.326
$n_r$ (S-I and S-II):	1.80	1.85	1.85	1.85	1.85	1.85	1.85	1.85	1.80
$n_i$ (S-I and S-II):	.022	.0215	.020	.019	.019	.017	.015	.012	.007
$\lambda$ ( $\mu\text{m}$ ):	.340	.414	.585	.610	.700	.800	.900	1.00	$\geq 1.50$
$n_r$ (S-I):	1.75	1.75	1.75	1.75	1.75	1.75	1.65	1.65	1.65
$n_r$ (S-II):	1.75	1.75	1.75	1.75	1.75	1.75	1.75	1.75	1.65
$n_i$ (S-I):	.0050	.0063	.0063	.0039	.0024	.0026	.0030	.0030	.0030
$n_i$ (S-II):	.0050	.0037	.0035	.0022	.0014	.0015	-	.0021	.0030

ORIGINAL PAGE IS  
OF POOR QUALITY.

## References

- Adams, J. B. and T. B. McCord, 1969: Interpretation of spectral reflectivity of light and dark regions. J. Geophys. Res., 74, 4851-4856.
- Ajello, J. M., K. D. Pang, A. L. Lane, C. W. Hord, and K. E. Simmons, 1976: Mariner 9 ultraviolet spectrometer experiment: Bright-limb observations of the lower atmosphere of Mars. J. Atmos. Sci., 33, 544-552.
- Allen, C. W., 1973: Astrophysical Quantities. 3rd Ed., London, Athlone Press, 310 p.
- Chandrasekhar, S., 1960: Radiative Transfer. New York, Dover Publications, 393 p.
- Conrath, B. J., 1975: Thermal structure of the Martian atmosphere during the dissipation of the dust storm of 1971. Icarus, 24, 36-46.
- Egan, W. G., T. Hilgeman, and K. D. Pang, 1975: Ultraviolet complex refractive index of Martian dust: Laboratory measurements of terrestrial analogs. Icarus, 25, 344-355.
- Gierasch, P. and R. Goody, 1972: The effect of dust on the temperature of the Martian atmosphere. J. Atmos. Sci., 29, 400-402.
- Joseph, J. H., W. J. Wiscombe, and J. A. Weinman, 1976: The delta-Eddington approximation. Submitted to J. Atmos. Sci.

- Leovy, C. B., G. A. Briggs, A. T. Young, B. A. Smith, J. B. Pollack, E. N. Shipley, and R. L. Wildey, 1972: The Martian atmosphere: Mariner 9 television experiment progress report. Icarus, 17, 373-393.
- Liou, K. N., 1974: Analytic two-stream and four-stream solutions for radiative transfer. J. Atmos. Sci., 31, 1473-1475.
- Mead, J. M., 1970: The contribution of atmospheric aerosols to the Martian opposition effect. Icarus, 13, 82-95.
- Moriyama, S., 1974: Effects of dust on radiation transfer in the Martian atmosphere: I. On infrared cooling. J. Meteor. Soc. Japan, 52, 457-462.
- Moriyama, S., 1975: Effects of dust on radiation transfer in the Martian atmosphere: II. Heating due to absorption of the visible solar radiation and importance of radiative effects of dust on the Martian meteorological phenomena. J. Meteor. Soc. Japan, 53, 214-220.
- Pang, K. D. and J. M. Ajello, 1976: Complex refractive index of Martian dust: Wavelength dependence and composition. To be published.
- Pang, K. D., J. M. Ajello, C. W. Hord, and W. S. Egan, 1976: Complex refractive index of Martian dust: Mariner 9 ultraviolet observations. Icarus, 27, 55-67.

- Pollack, J. B., O. B. Toon, and B. N. Khare, 1973: Optical properties of some terrestrial rocks and glasses. Icarus, 19, 372-389.
- van de Hulst, H. C., 1974: The spherical albedo of a planet covered with a homogeneous cloud layer. Astron. & Astrophys., 35, 209-214.
- de Vaucouleurs, G., 1964: Geometric and photometric parameters of the terrestrial planets. Icarus, 3, 187-235.

Table I

Isotropic single scattering albedo  $\tilde{\omega}_*$  estimated from the Mariner 9 TV observations of limb haze over the Martian tropics. It has been assumed that  $\tau_N \geq 1$ . (E. Anderson, communicated by C. B. Leovy.)

$\beta$ -Camera Filter	Effective Wavelength	$\tilde{\omega}_*$
Violet	.414 $\mu$ m	0.62 $\pm$ .05
Orange (1)	.585 $\mu$ m	0.72 $\pm$ .04
Orange (2)	.610 $\mu$ m	0.81 $\pm$ .05

TABLE II

Parameters used in Eq. 3 to generate size distributions for the solar heating calculations. These parameters are within ranges established by Pang et al. (1976). The geometrical cross-sectional area per particle, calculated from Eq. 3c, is also listed.

---

S-I :	$a = 1.0 \mu m$	$b = 0.4$	$G = 0.376 \mu m^2$
S-II:	$a = 1.5 \mu m$	$b = 0.25$	$G = 2.649 \mu m^2$

---

ORIGINAL PAGE IS  
OF POOR QUALITY

TABLE III

Solar heating rates per unit mass ( $\text{mw gm}^{-1}$ ) for a uniformly mixed dusty atmosphere.

S-II, AS-II, $\tau_N = 1.5$			Cos (solar zenith angle) = $\mu_0$						Average over $\mu_0$
p(mb)	z(scale ht.)	$\tau(\lambda = .586\mu\text{m})$	0.2	0.4	0.6	0.8	0.9	1.0	
.333	2.7	0.1	.52	.66	.74	.80	.82	.85	.58
2.0	0.92	0.6	.22	.47	.64	.77	.83	.88	.45
5.0	0.	1.5	.10	.29	.49	.68	.77	.86	.36
S-I, AS-II, $\tau_N = 0.15$									
.333	2.7	0.01	.061	.068	.074	.080	.083	.086	.063
2.0	0.92	0.06	.054	.065	.073	.080	.084	.087	.059
5.0	0.	0.15	.044	.060	.071	.080	.085	.089	.054



TABLE IV

Radiative fluxes, shown as per cent of the incident solar radiation, for a uniformly mixed dusty atmosphere.

S-II, AS-II, $\tau_N = 1.5$	Cos (solar zenith angle) = $\mu_0$						Average over $\mu_0$
	0.2	0.4	0.6	0.8	0.9	1.0	
$\hat{Q}_m = F_{NET}(\tau_N) - F_{NET}(0)$	25%	24%	21%	19%	19%	18%	21%
$F\uparrow(0)$	52%	45%	40%	36%	34%	33%	39%
$F_{SFC} = -F_{NET}(\tau_N)$	23%	31%	39%	45%	47%	49%	40%
$\pi I_S$ (mw cm <sup>-2</sup> )	12.9	25.8	38.8	51.7	58.1	64.6	32.3
S-I, AS-II, $\tau_N = 0.15$							
$\hat{Q}_m = F_{NET}(\tau_N) - F_{NET}(0)$	6%	3%	2%	2%	2%	2%	3%
$F\uparrow(0)$	43%	40%	38%	37%	37%	37%	38%
$F_{SFC} = -F_{NET}(\tau_N)$	51%	57%	60%	61%	61%	61%	59%

ORIGINAL PAGE IS  
OF POOR QUALITY .

## List of Figures

- Figure 1 Real and imaginary parts of the complex refractive index  $m = m_r - im_i$ . The points (+) were taken from Pang and Ajello (1976). The points (o) are for a basalt sample studied by Egan et al. (1975); the points (x) are for a similar sample studied by Pollack et al. (1973). The remaining  $m_i$  points were evaluated using the two different size distributions listed in Table II. The points ( $\phi$ ) are based on the Mariner 9 TV data while the points ( $\square$ ) are based on the planetary geometric albedo. The  $m_r$  values are consistent with Mead's (1970) work.
- Figure 2 Generating the isotropic and non-isotropic single scattering albedos for  $\lambda = .586 \mu\text{m}$  as a function of the imaginary component of the refractive index. Four size distributions were used: solid lines are for an effective radius  $a = 1.0 \mu\text{m}$ , dashed lines for  $a = 1.5 \mu\text{m}$ , while (o) indicates an effective variance  $b = 0.4$ . Otherwise,  $b = 0.25$ . (The parameters  $a$ ,  $b$  were used in the formula given by Eq. (3) with  $N = 1$  particle per unit volume.)  $m_r = 1.65$ .

- Figure 3      Geometric and Bond albedos,  $A_G$  and  $A_B$ , respectively, as a function of the isotropic single scattering albedo  $\tilde{\omega}_*$  in a homogeneous, isotropic, semi-infinite medium. The phase integral  $IP = A_B/A_G$  is also shown.
- Figure 4      Single scattering albedo  $\tilde{\omega}_0$  generated from different sources by various methods using the S-II size distribution.
- Figure 5      Single scattering albedo  $\tilde{\omega}_0$  generated from different sources by various methods using the S-I size distribution.
- Figure 6      The ground albedo constructed assuming that the airborne dust is optically the same as the dust on the surface. The circles (o) are for the ground albedo estimated (by linear interpolation) at the quadrature points used for the integration over the solar spectrum. Collectively these are designated AS-II. The upper curves show  $\tilde{\omega}_0$  at the quadrature points as calculated for the S-I and S-II size distributions using the refractive indices shown in Fig. 1. These points have been joined by straight line segments to show the general trend.

ORIGINAL PAGE IS  
OF POOR QUALITY

Figure 7      Solar heating per unit optical depth as a function of  $\tau$ , the optical depth at  $\lambda = .586\mu\text{m}$ , and  $\mu_0$ , the cosine of the solar zenith angle.  $Q_\tau(\Delta_s)$  has been computed for S-II optical parameters and various combinations of surface albedo  $A_s$  and total optical depth  $\tau_N$ . The units are  $1 \text{ mw} = 10^4 \text{ ergs sec}^{-1}$ . Integration over wavelength was accomplished by using a 32 point Gauss-Legendre quadrature over  $\ln \lambda$ .

Figure 8      Contributions to the total solar heating (integrated over  $\Delta_s$ ) from the following regions:

$$\Delta_{UV} : 0.2 \leq \lambda \leq 0.31\mu\text{m}$$

$$\Delta_{NUV} : 0.31 \leq \lambda \leq 0.4\mu\text{m}$$

$$\Delta_{VIS} : 0.4 \leq \lambda \leq 1.0\mu\text{m}$$

$$\Delta_{NIS} : 1.0 \leq \lambda \leq 2.5\mu\text{m}$$

$$\Delta_s : 0.2 \leq \lambda \leq 5.0\mu\text{m}$$

The effects of the lower boundary conditions given by Eqs. 14 and 16 are also shown. The heating rates were computed for  $\mu_0 = 1.0$  and S-II optical parameters. The contributions for the various regions were obtained by summing the values for those quadrature points falling in the specified region  $\Delta_\lambda$ .

- Figure 9 Contributions to the total solar heating rates from the same spectral regions as defined in Fig. 8. Calculations were done for  $\mu_0 = 1.0$ ,  $\tau_N = 1.5$ , and for both the S-I and S-II optical parameter sets. The surface albedo used was taken from Fig. 6.
- Figure 10 The effect of surface albedo on the total solar heating rate for various  $\mu_0$  values as a function of optical depth. Calculations were done for  $\tau_N = 1.5$  and for S-II optical parameters.
- Figure 11 The layer heating rate  $\hat{Q}_\tau$  as a function of zenith angle for both  $\tau_N = 1.5$  and  $\tau_N = 0.15$ . The effects of various optical parameter sets and surface albedos are shown.
- Figure 12 Same as Fig. 7, except that  $\tau_N = 0.15$  is the "finite" optical depth and the S-I parameter set was used.
- Figure 13 Comparing the contributions to the total heating from various spectral regions when  $\mu_0 = 1.0$  and  $\tau_N = 0.15$ . The effect of replacing the albedo from Fig. 6 by a constant  $A_s = 0.3$  value is shown. Note that when  $A_s = 0.3$ , the  $\Delta_{\text{NUV}}$  contribution is indistinguishable from the  $\Delta_{\text{NIR}}$  contribution.

Figure 14      Solar heating rates per unit mass as a function of height for an atmosphere in which dust is uniformly mixed and  $\tau_N = 1.5$  (at  $p_s = 5$  mb). The calculation used the S-II optical parameters and AS-II ground albedo. The broken line shows the value of the solar heating rate (per unit mass) averaged over  $\mu_0$ .

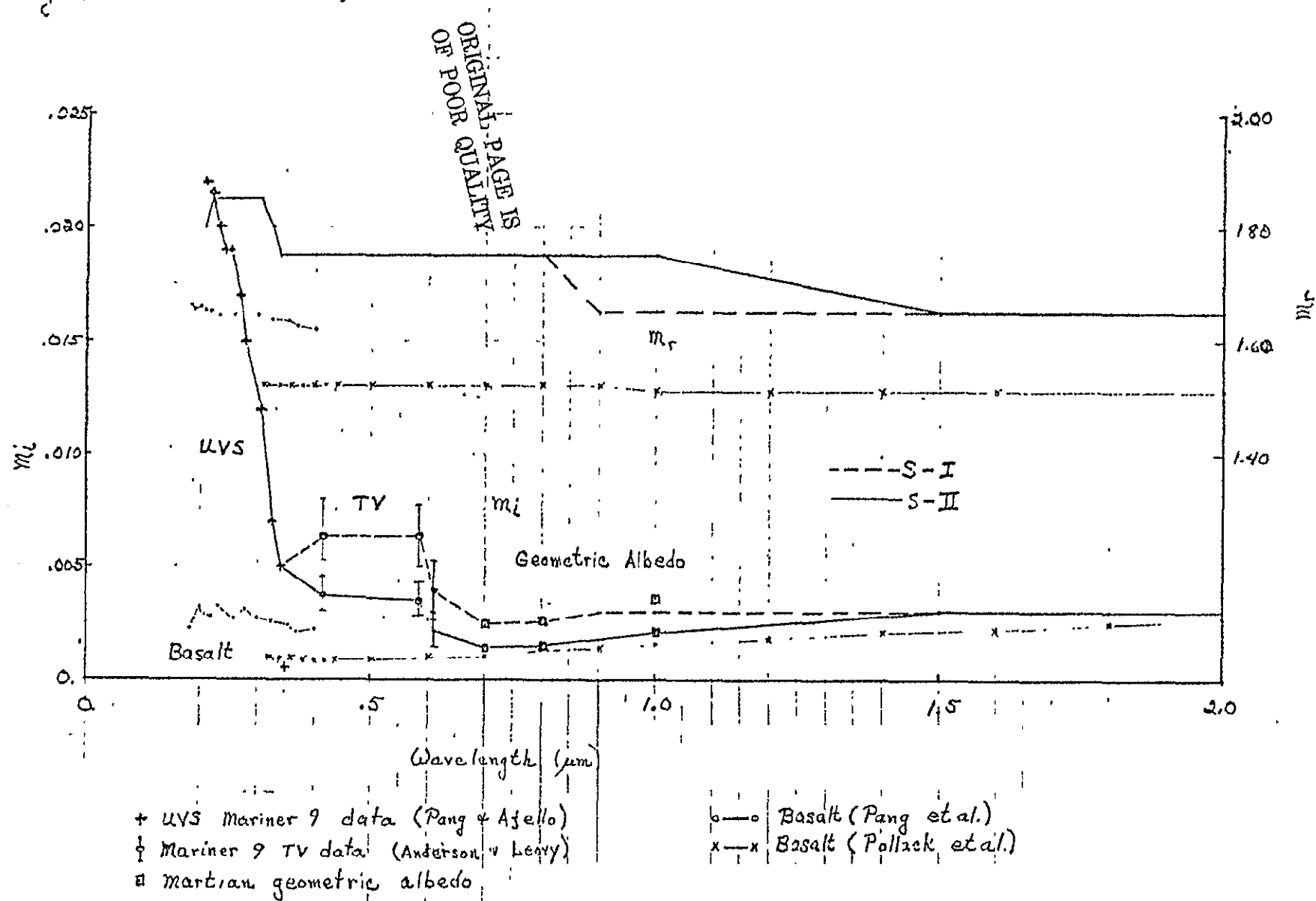
Figure A-1      Comparing different approximations to the radiative transfer equation with the Doubling method for  $\lambda = .586\mu\text{m}$ ,  $A_s = .2788$ , and  $\mu_0 = 1.0$ . The plotted quantity is the divergence of the net flux with respect to the optical depth at  $\lambda = .586\mu\text{m}$ . The solar flux (SF) has been arbitrarily set equal to one. The total optical depth is  $\tau_N = 1.5$ , and the optical parameters were computed from the S-II size distribution.

_____	Doubling method
.-.-.-.-.	DE ( $f = g^2$ )
— — —	DE ( $f = \omega_2/5$ )
— - —	FS (4-stream discrete ordinate method)
-----	FMS (4-stream multiple average-intensity method)

ORIGINAL PAGE IS  
OF POOR QUALITY

- Figure A-2 Same as Fig. A-1 except  $\mu_0 = 0.9$ .
- Figure A-3 Same as Fig. A-1 except  $\mu_0 = 0.6$ .
- Figure A-4 Same as Fig. A-1 except  $\mu_0 = 0.2$ .
- Figure A-5 Relative differences (in %) of the radiative transfer approximations when compared against the Doubling method for computing the heating rate for the entire layer, defined as
- $$\hat{Q}_\tau = \int_0^{\tau_N} dF_{\text{NET}}/d\tau = F_{\text{NET}}(\tau_N) - F_{\text{NET}}(0)$$
- $\hat{Q}_\tau$  is shown as a function of  $\mu_0$ , the cosine of the solar zenith angle. The calculations were done for  $\tau_N = 1.5$ ,  $\lambda = .586\mu\text{m}$ ,  $A_s = .2788$ , and the S-II set of optical constants.
- Figure A-6 Same as Fig. A-5, except the quantity being plotted is the net flux at the surface ( $\tau_N = 1.5$ ).
- Figure A-7 Same as Fig. A-5, except the quantity being plotted is the upward flux  $F_i(0)$  from the dust layer.
- Figure A-8 Same as Fig. A-1 except plotted for  $A_s = 0.3$  and  $\lambda = .201\mu\text{m}$ .
- Figure A-9 Comparing different radiative transfer approximations with the Doubling method for  $dF_{\text{NET}}/d\tau$  generated using the S-I optical constants,  $\tau_N = 0.15$  and  $A_s = 0.2788$  for  $\lambda = .586\mu\text{m}$ .
- Figure A-10 Same as Fig. A-5, except computed using the S-I optical constants and for  $\tau_N = 0.15$ .

Fig 1.





ORIGINAL PAGE IS  
OF POOR QUALITY

12-153 10

Fig 2.

Size Distributions

$a = 1.0 \mu m$

$a = 1.5 \mu m$

Circles  $\circ$   $b = 0.4$

Dots  $\cdot$   $b = 0.25$

$$\tilde{\omega}_* = \frac{\tilde{\omega}_0 - \tilde{\omega}_0 g}{1 - \tilde{\omega}_0 g}$$

where

$g \equiv$  asymmetry factor

$\tilde{\omega}_0 \equiv$  single scattering albedo

$m_r = 1.65$

$\lambda = .585 \mu m$

Amplitude of  $\tilde{\omega}_*$

$\tilde{\omega}_0$

$\tilde{\omega}_*$

$m_i$  (Imaginary part of refractive index)

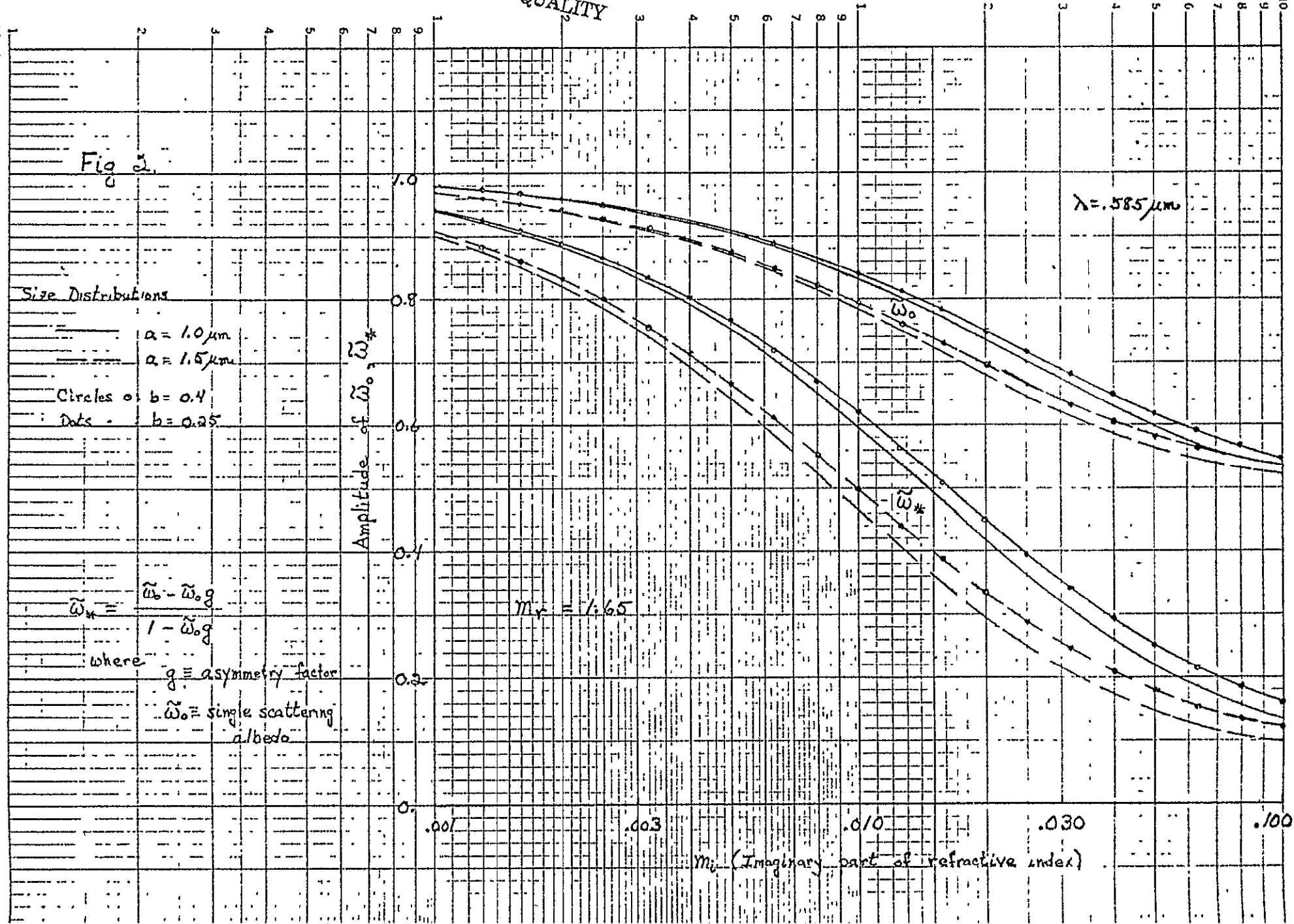
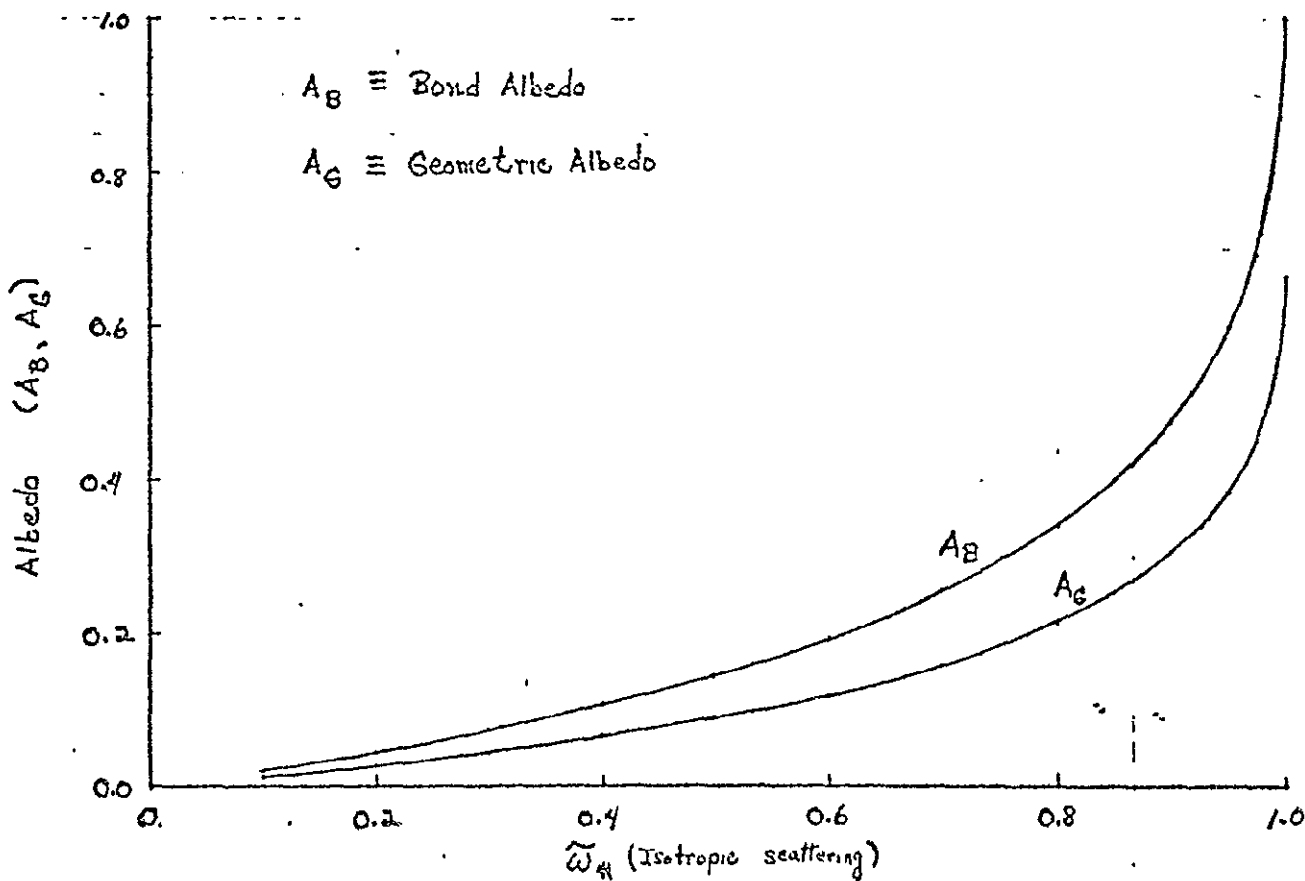
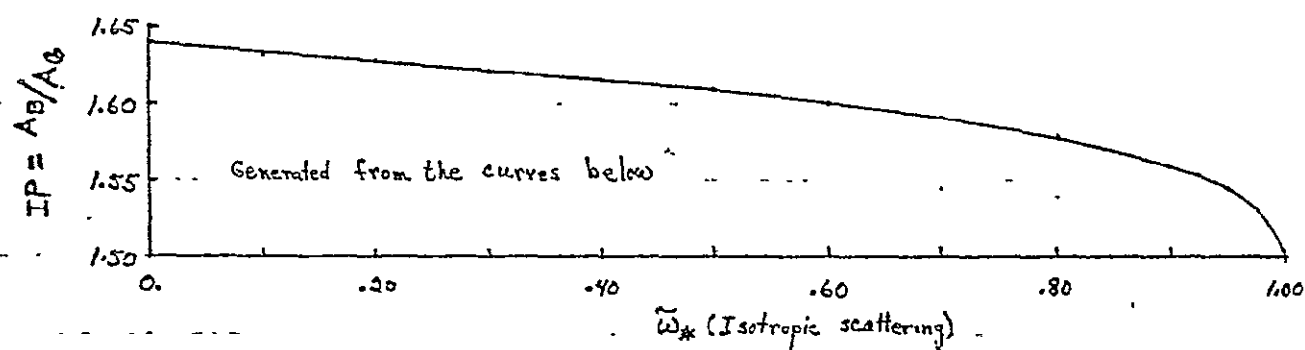
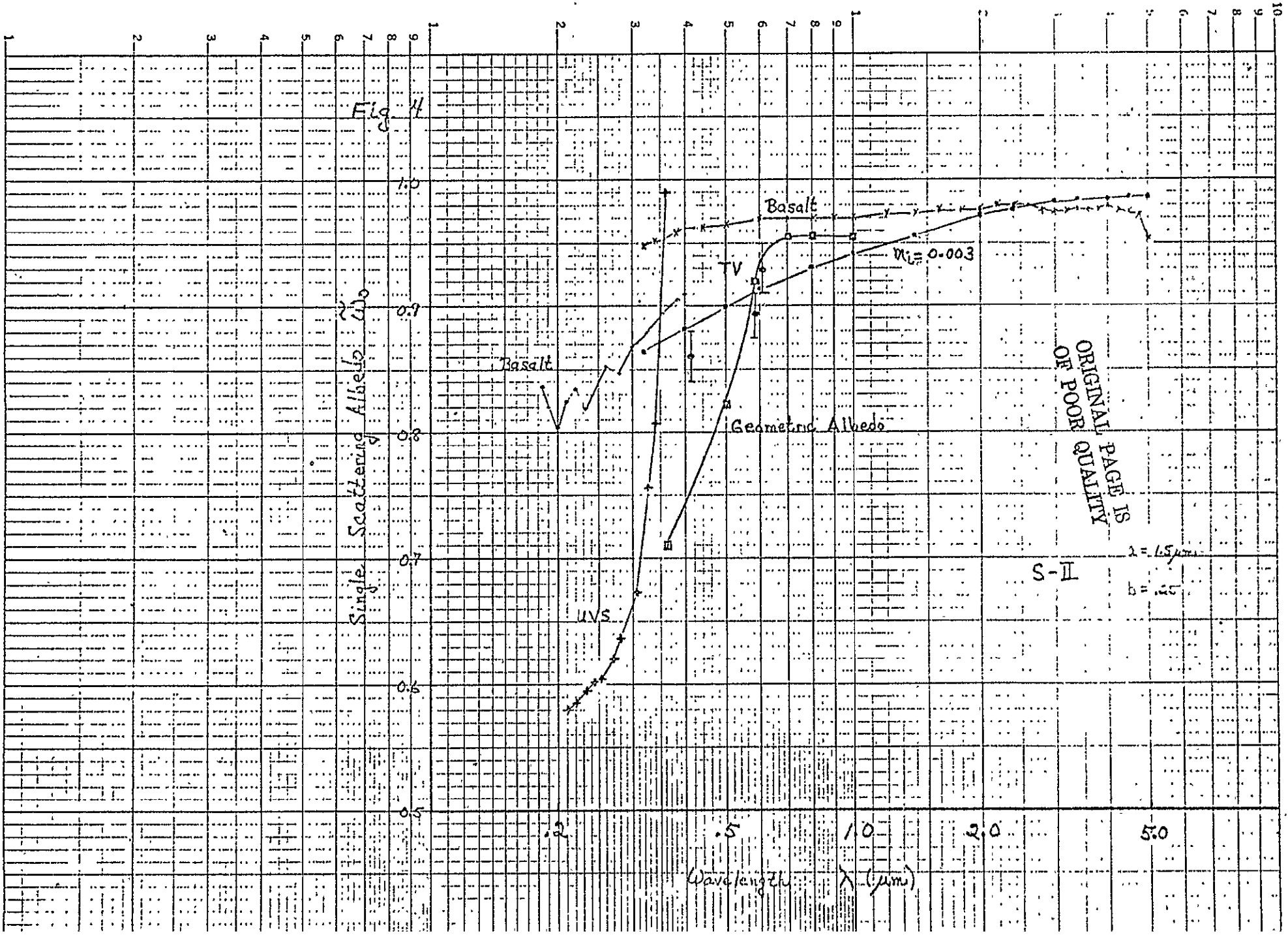


Fig. 3.



Vertical distance  
1 inch = 10 to the inch



ORIGINAL PAGE IS  
OF POOR  
QUALITY

S-II

$\lambda = 1.5 \mu m$   
 $b = .25$

Fig 5

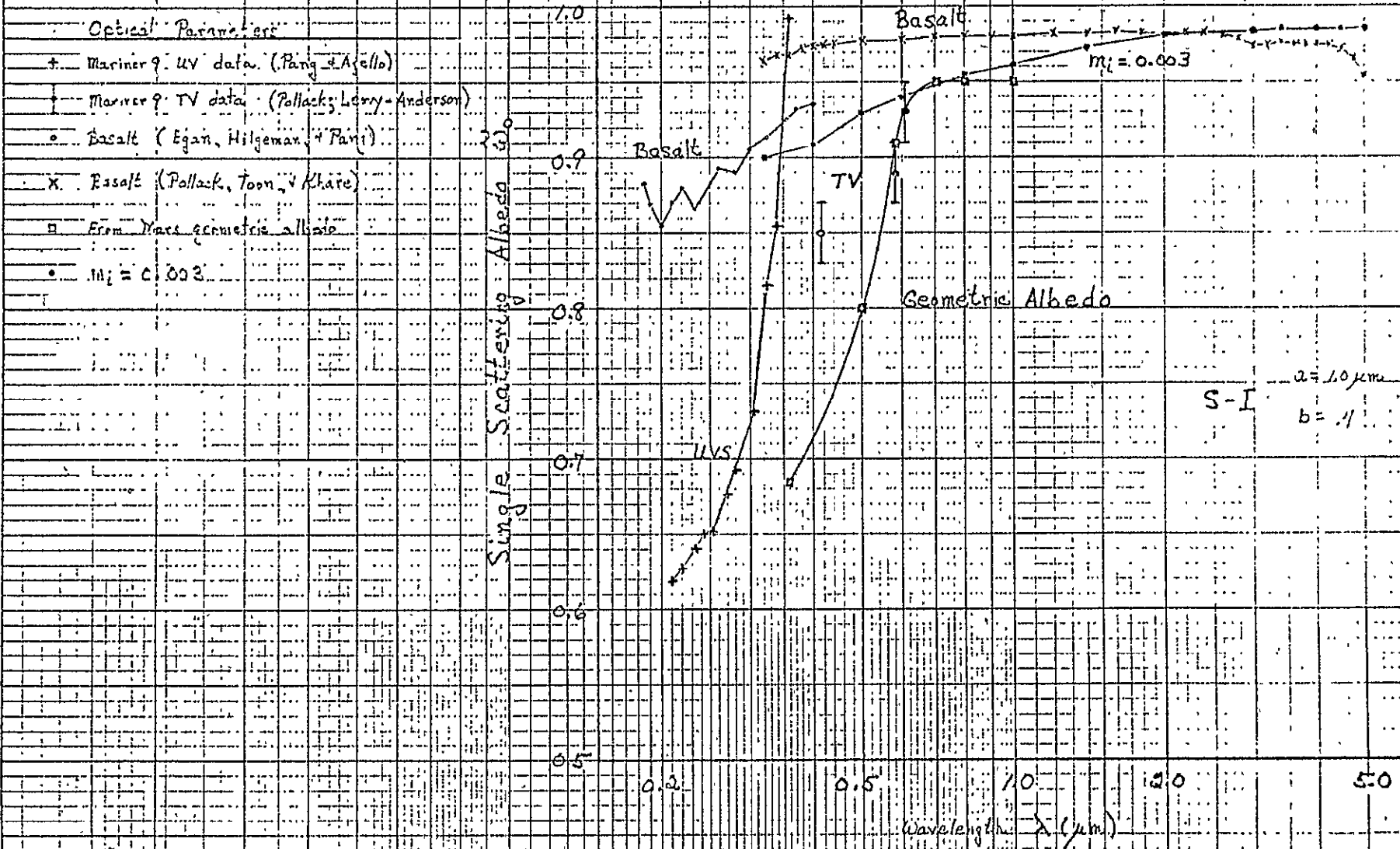


Fig. 6

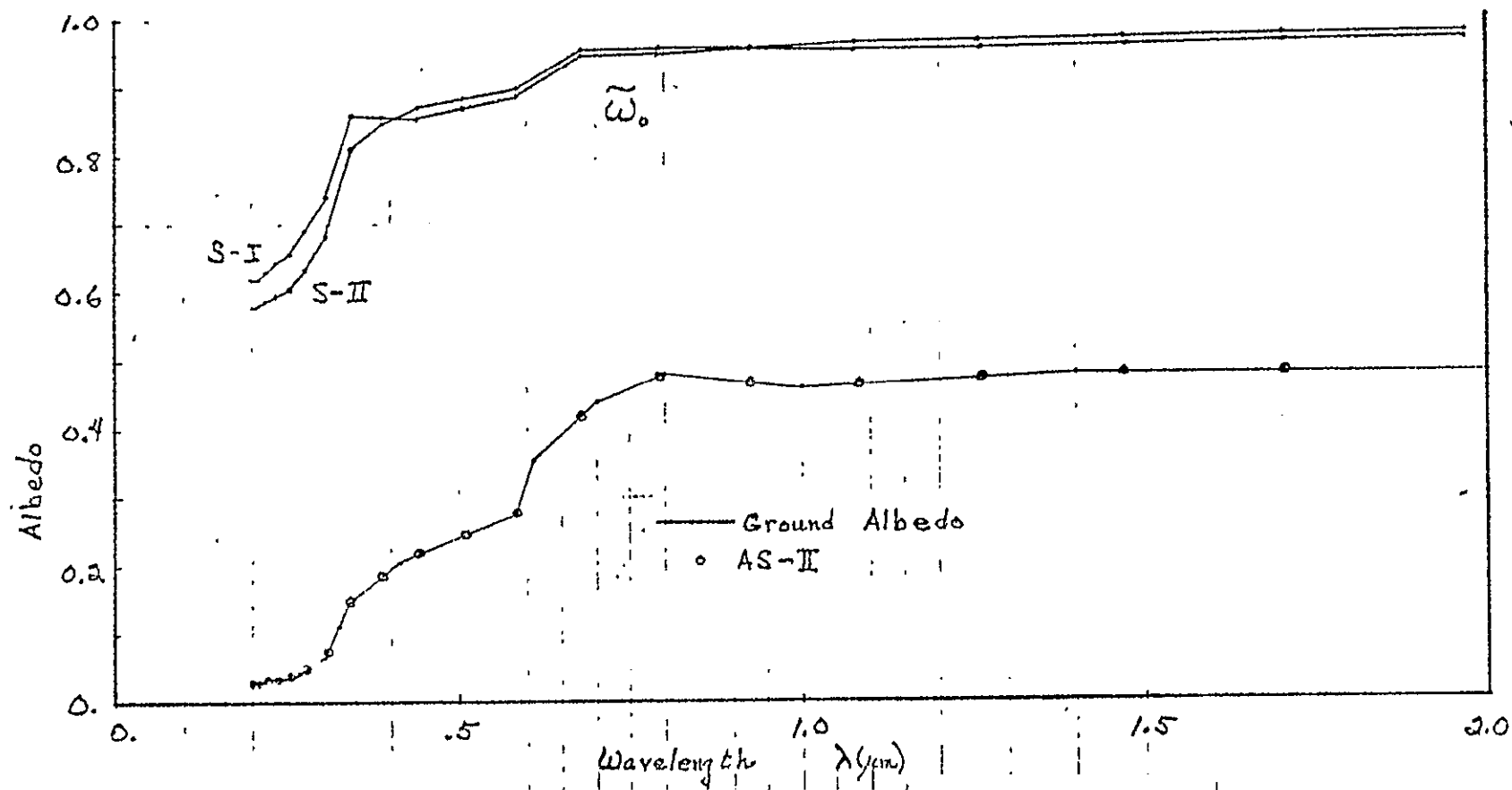
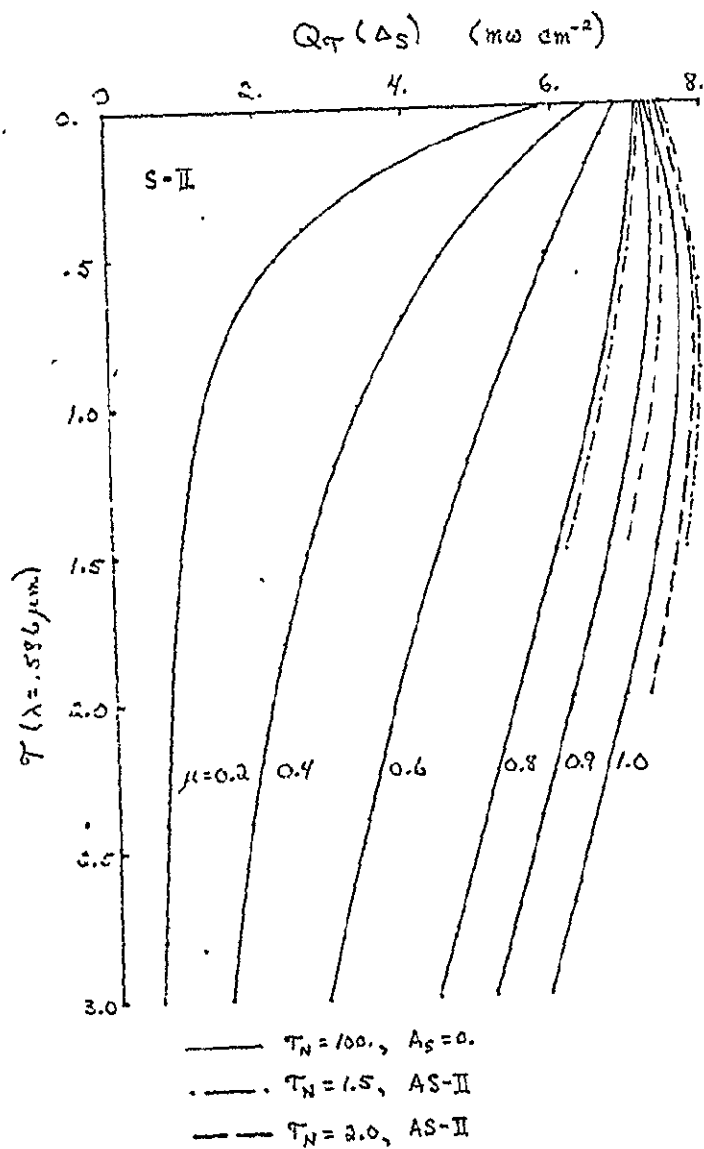


Fig. 7



ORIGINAL PAGE IS  
OF POOR QUALITY

Fig. 8

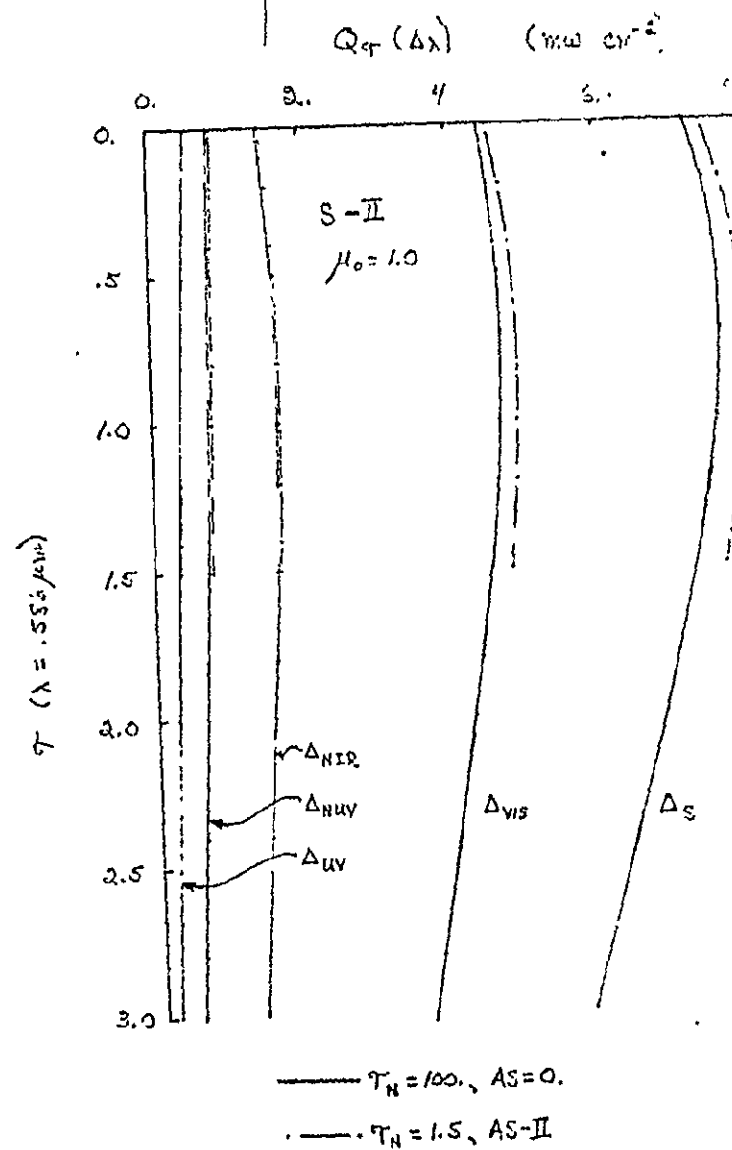


Fig. 9

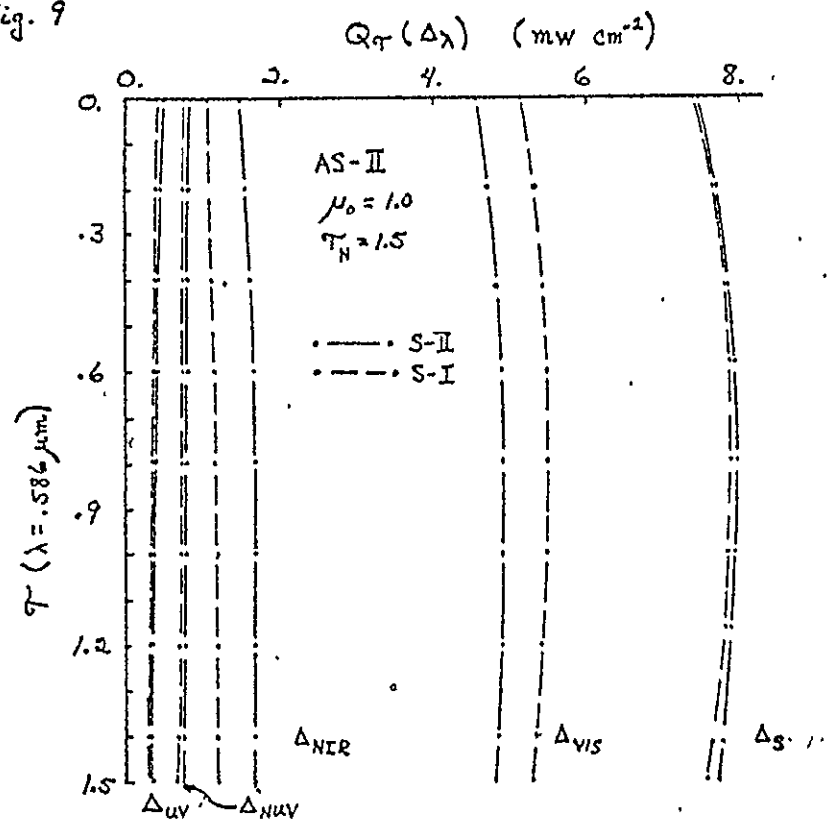


Fig. 10

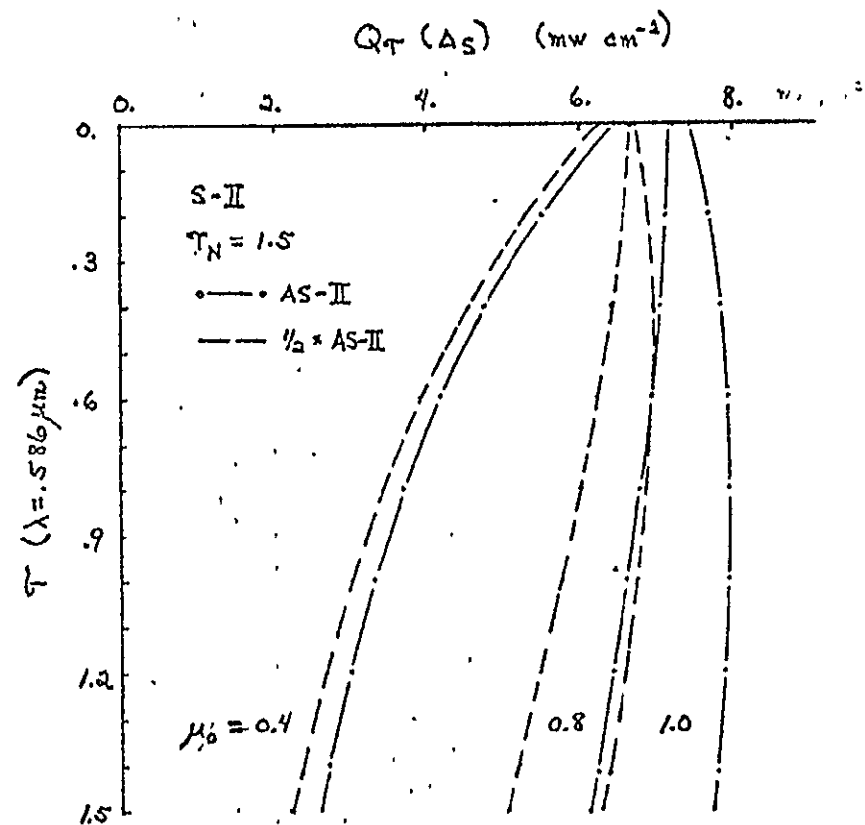
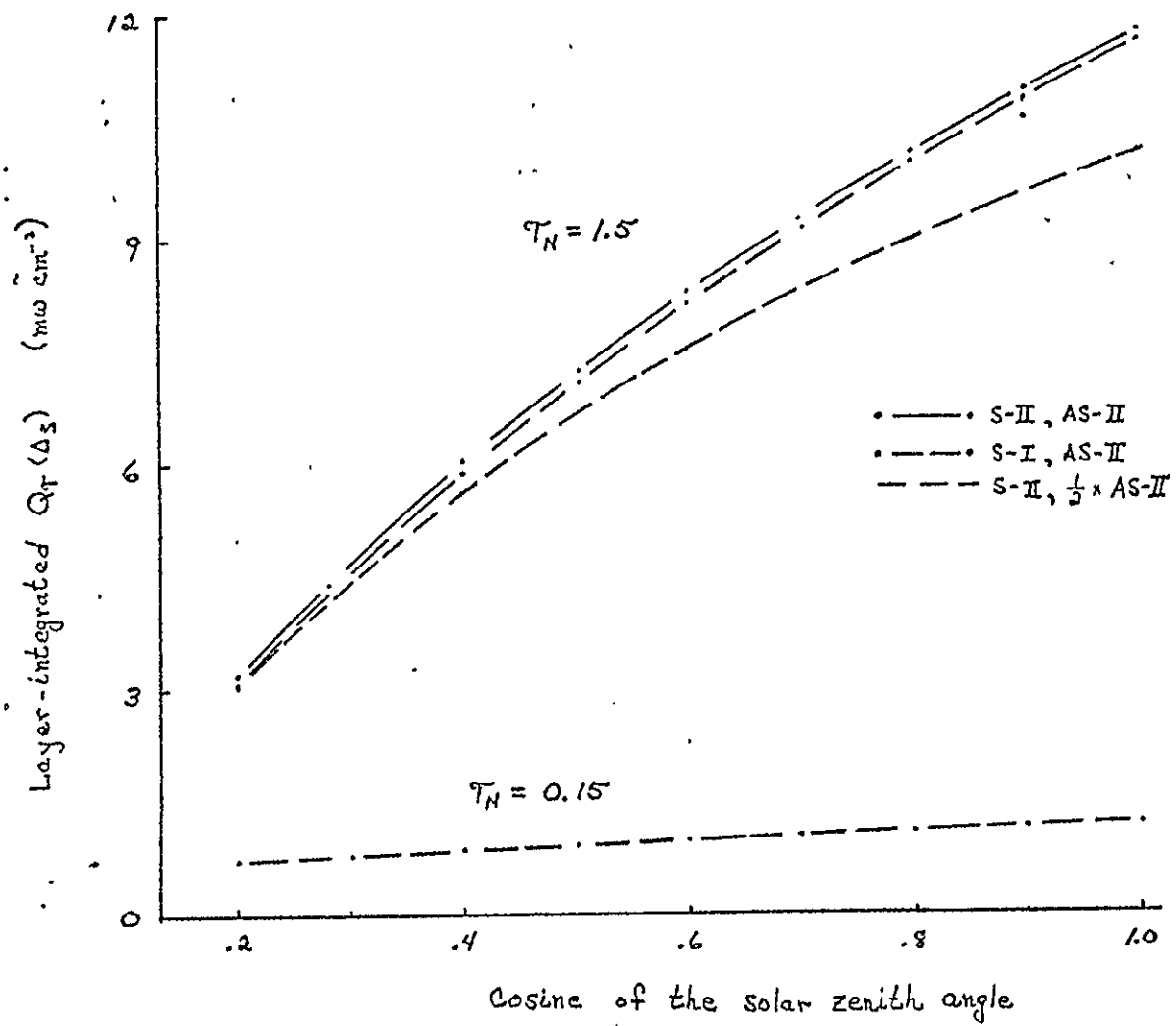


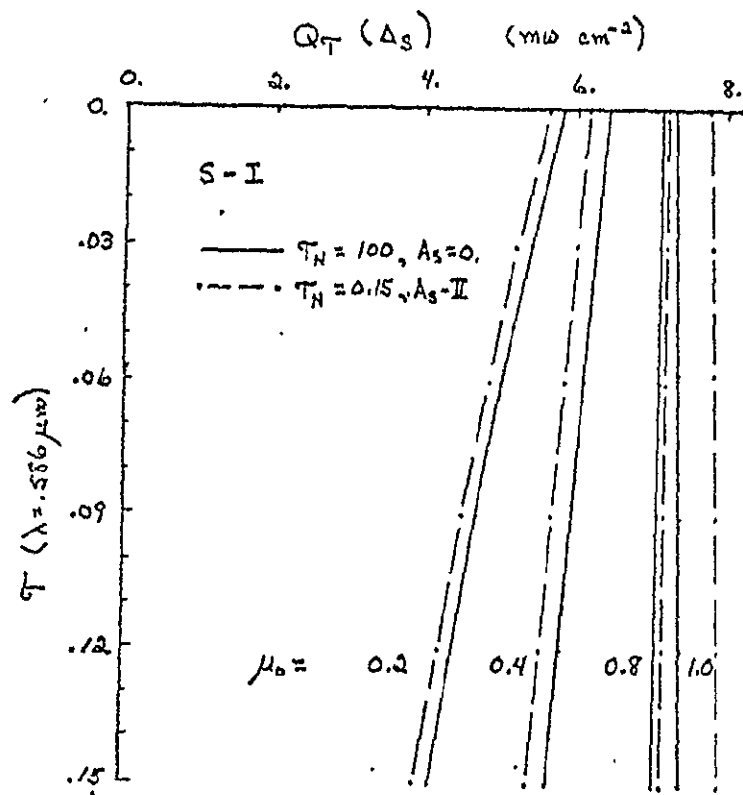
Fig. 11



ORIGINAL PAGE IS  
OF POOR QUALITY



Fig. 12



ORIGINAL PAGE IS  
OF POOR QUALITY.

Fig. 13

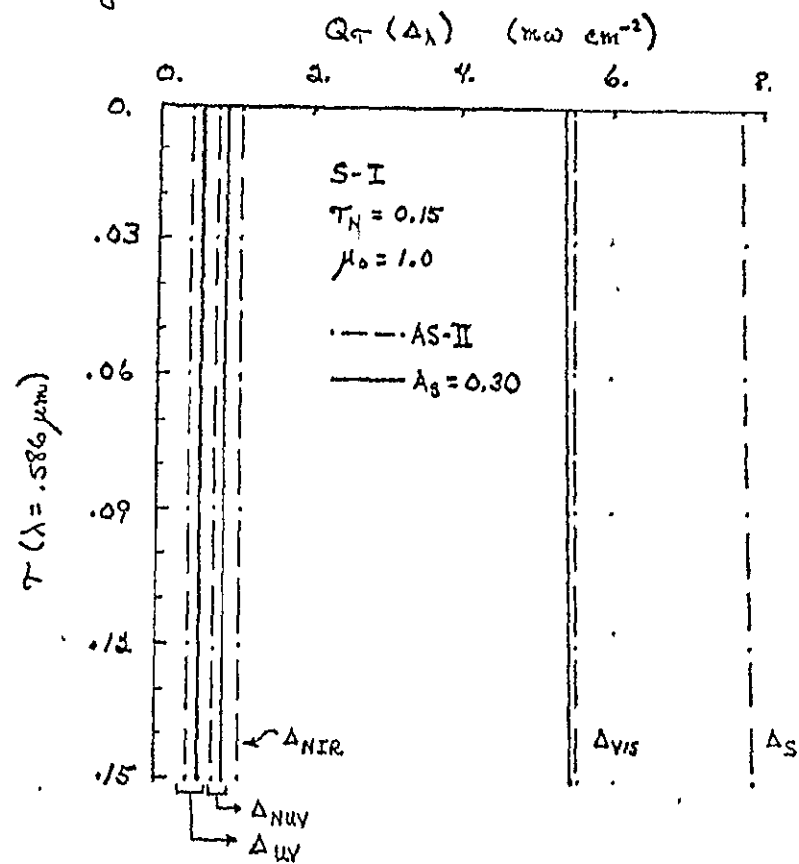


Fig 14

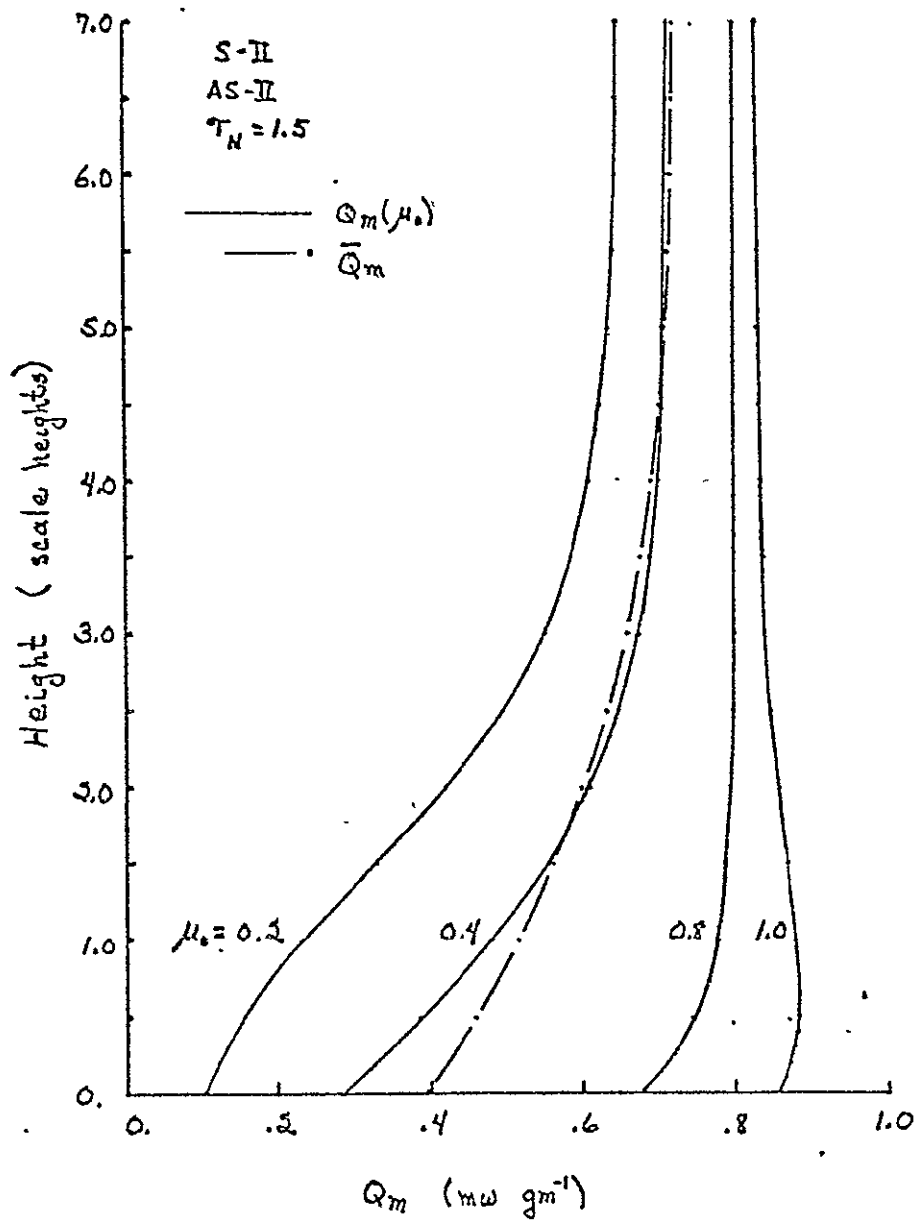


Fig A-1

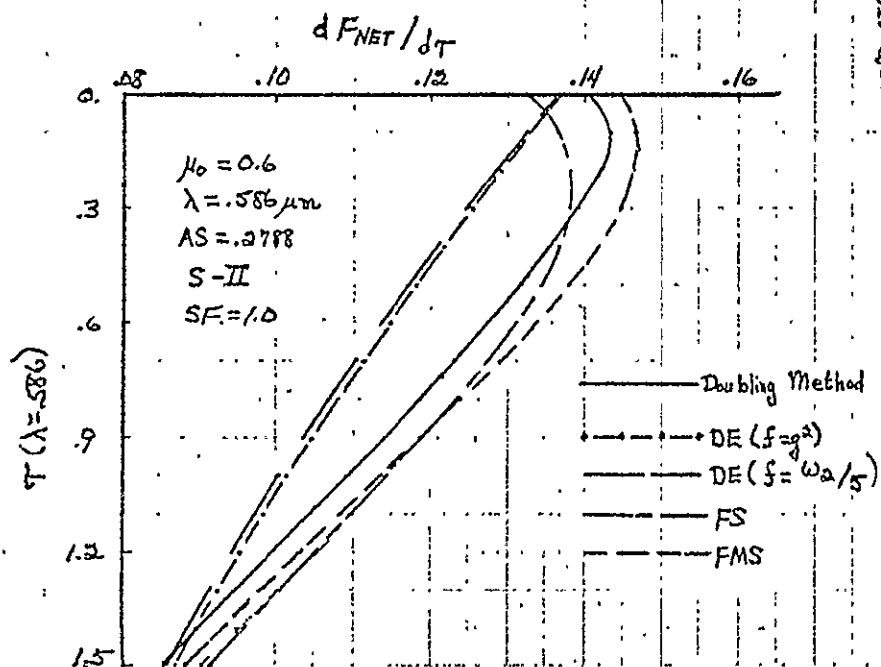
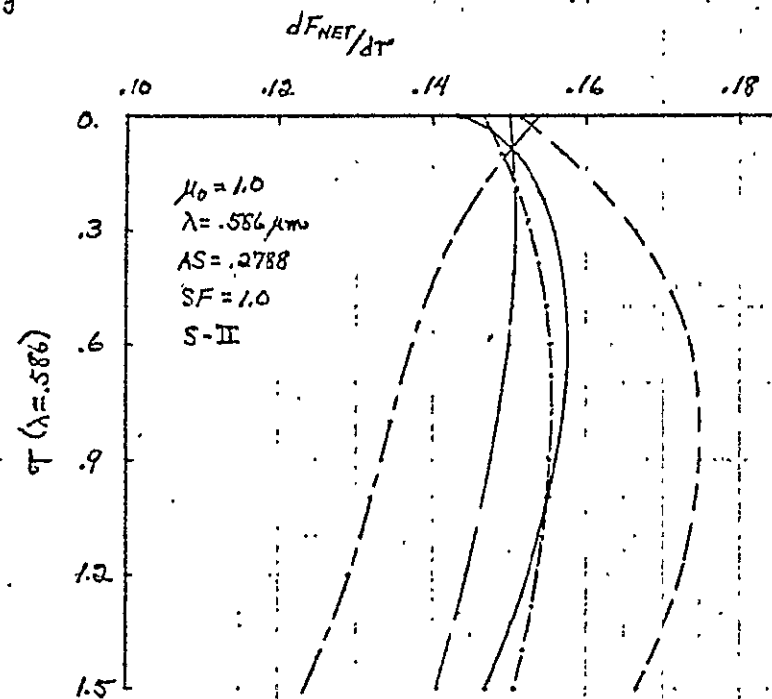


Fig A-2

Fig A-3

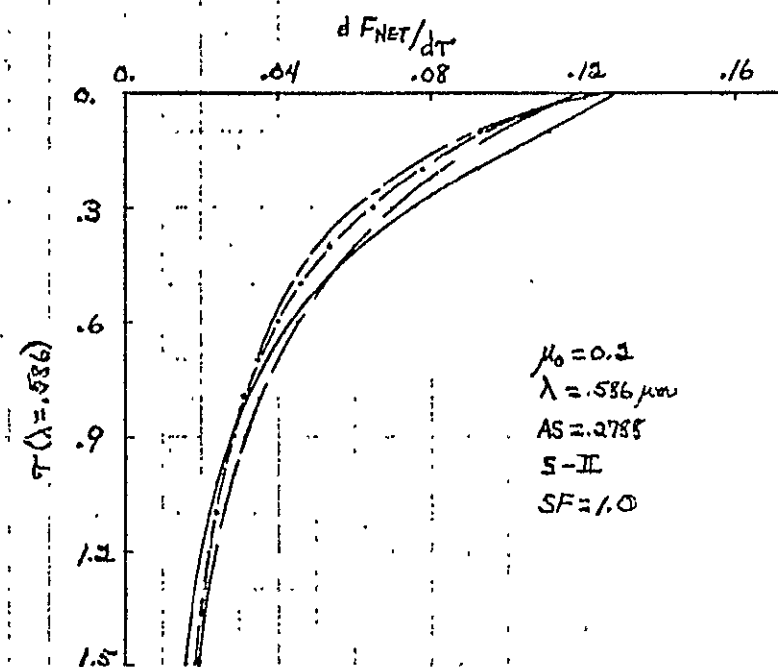
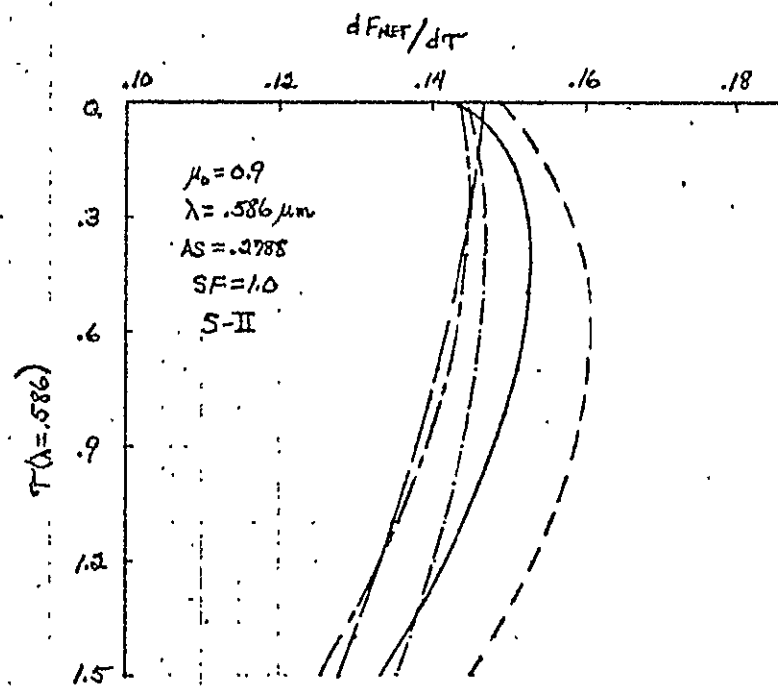


Fig A-4

ORIGINAL PAGE IS  
OF POOR QUALITY

Fig A-5

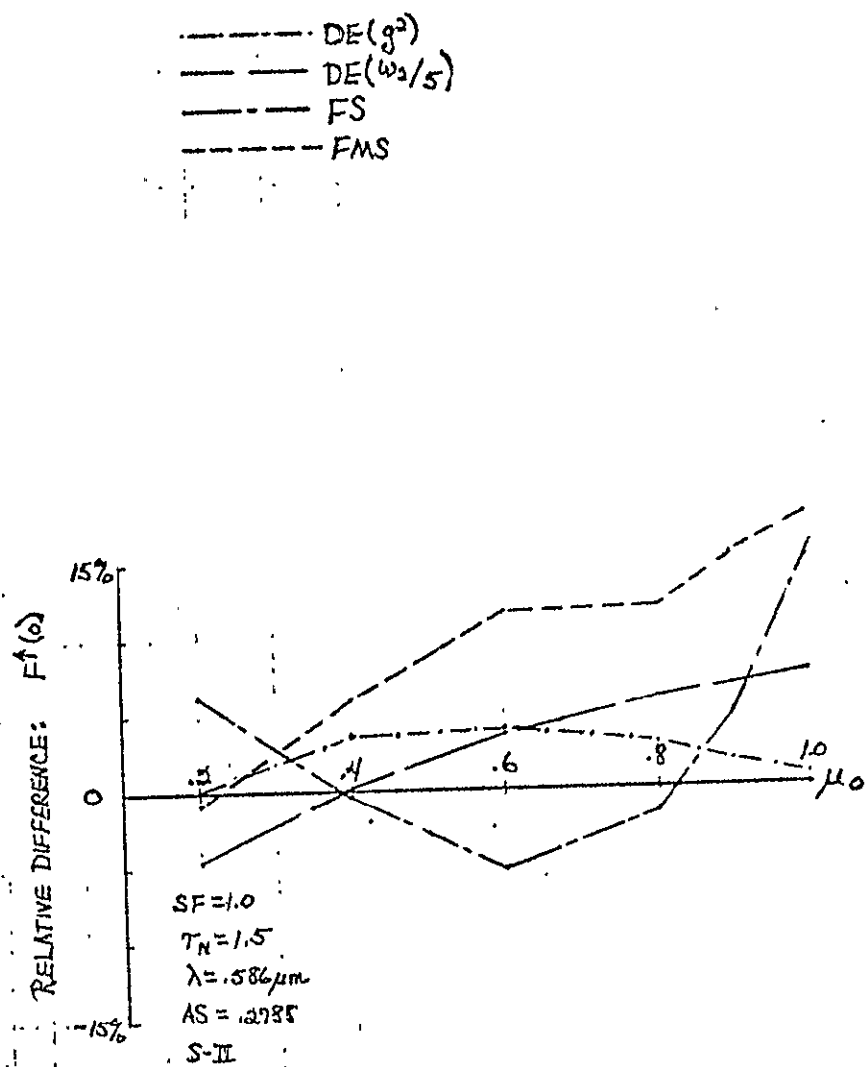
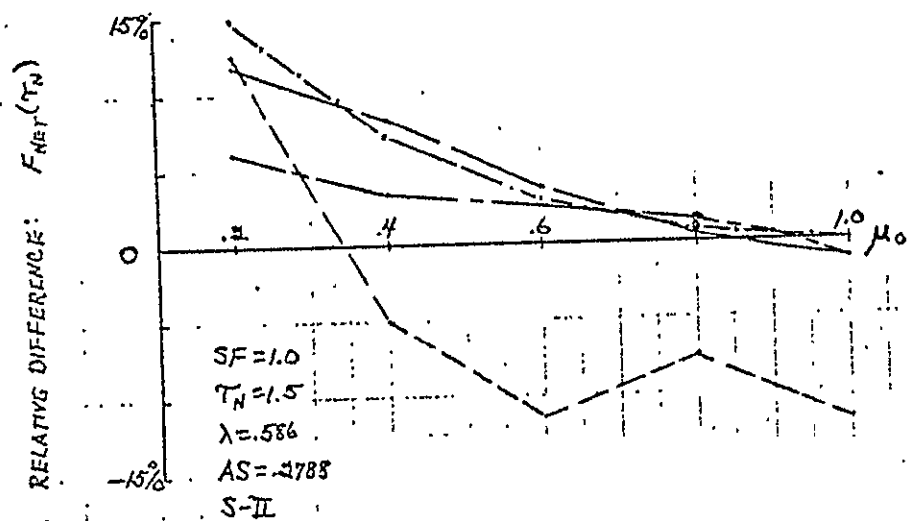
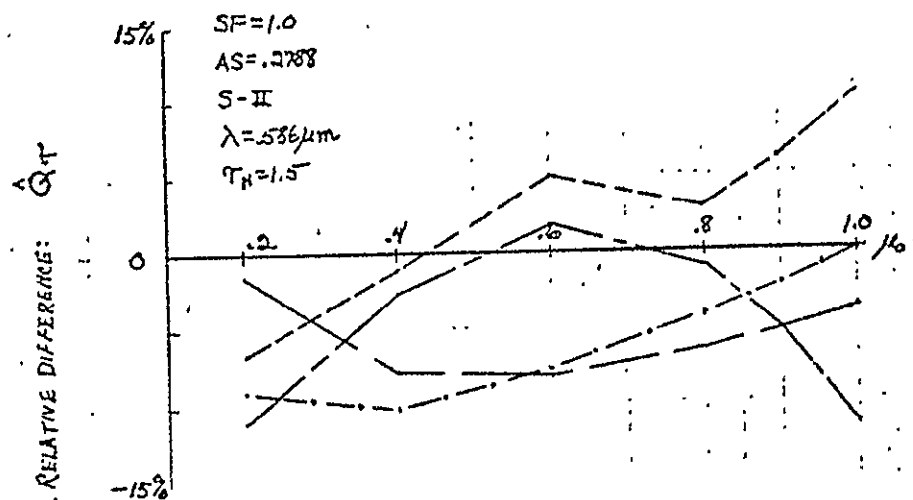


Fig A-8

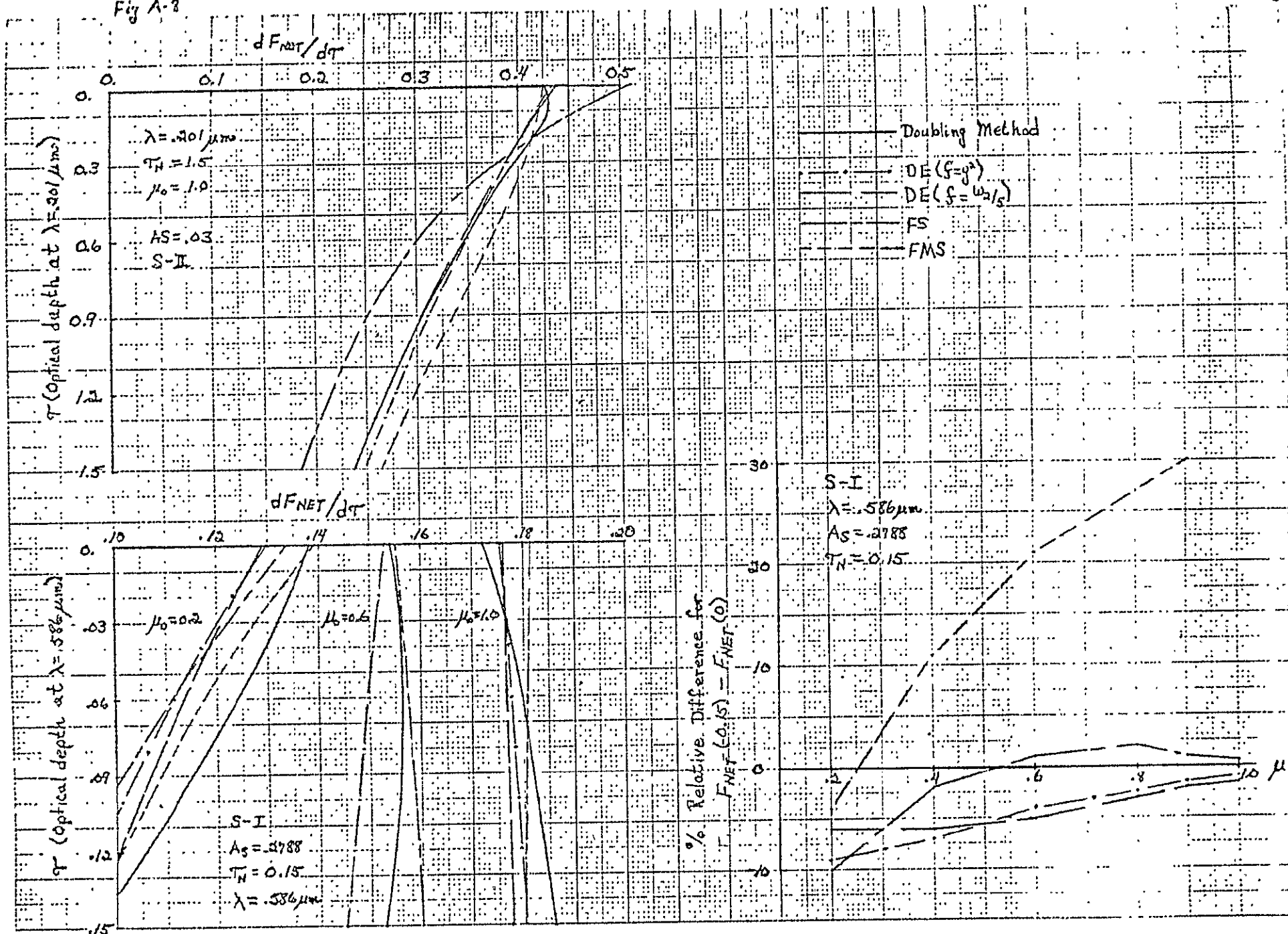


Fig A-9

ORIGINAL PAGE IS  
OF POOR QUALITY

Fig A-10